Applied Thermal Engineering 229 (2023) 120642

Contents lists available at ScienceDirect

Applied Thermal Engineering

journal homepage: www.elsevier.com/locate/apthermeng

Research Paper

Multi-objective optimisation of MOF-801 adsorbent packed into copper foamed bed for cooling and water desalination systems

Mohamed Rezk [a], Mahmoud B. Elsheniti [a,b,*], Ahmed Rezk [c,*], Osama A. Elsamni [a]

[a] Mechanical Engineering Department, Faculty of Engineering, Alexandria University, El-Chatby, Alexandria 21455, Egypt
[b] Mechanical Engineering Department, College of Engineering, King Saud University, Riyadh 11451, Saudi Arabia
[c] Energy and Bioproducts Research Institute (EBRI), College of Eng. and Physical Science, Aston University, Birmingham B4 7ET, UK

ARTICLE INFO

Keywords:
Copper foam
MOF-801
Silica gel
Adsorption cooling
Desalination
Global optimisation

ABSTRACT

Recently, there have been several endeavours to enhance the performance of the adsorption systems for cooling cum desalination by developing new materials and adsorbent bed designs. Therefore, this article contributes to the field by computationally studying the utilisation of state-of-the-art MOF-801 adsorbent packed into the emerging copper-foamed adsorbent bed heat exchanger and benchmarking its performance against that utilising silica gel baseline adsorbent. A multi-objective global optimisation aimed simultaneously at the best coefficient of performance, specific cooling power, and clean water productivity was undertaken. The optimisation was built on the insights from a broad parametric study for the geometric and operating conditions. Given the novelty of the adsorbent MOF-801 and bed design combination, a one-dimensional model was developed to imitate the heat transfer in the adsorbent bed and coupled with a previously validated empirical lumped analytical model for the adsorption system using the MATLAB platform. Using copper foam significantly enhanced the effective thermal performance of the adsorbent bed, improving the overall system performance under different operating conditions. Furthermore, the clean water productivity of the MOF-801-based system outperformed that of the SG-based system by 38%, as the former yielded 29.7 m^3/(ton.day), while the latter 21.5 m^3/(ton.day). Besides, the MOF-801-based system showed specific cooling power of 830.8 W/kg compared to 611.5 W/kg for the silica gel-based system. However, the cooling capacity per unit volume determined the systems' form factor, and the coefficient of performance was respectively higher by 9.6% and 20.2% for the silica gel-based system than those of the MOF-801-based system, stemming from the low packing density of MOF-801.

1. Introduction

Due to economic and population expansion, many parts of the world are experiencing increasing demand for fresh water and restrictions on energy resources and their consumption. Climate change and global warming have also directed attention to utilising new environmentally friendly technologies for fresh water and cooling production systems. It was reported that the world will likely face a 40% water shortage by 2030 [1], and around 52% of the world's population is expected to live in water-stressed areas by 2050 [2,3]. As freshwater resources dwindle, more energy-intensive clean water production methods, such as thermal, reverse osmosis and chemical desalination, become imperative [4,5]. However, the energy consumed by these systems, typically between 3.5 and 12 kWh/m^3, dramatically increases the running cost and CO_2 emissions [6,7]. As such, the total energy consumption in the water sector is predicted to double by 2040 [8].

Regarding cooling applications, numerous refrigeration technologies, dominated by vapour compression systems, have been developed. Of these applications, space cooling is the fastest growing and is predicted to share 30% of the energy consumption by 2050 [9]. Besides, conventional vapour compression systems utilise harmful refrigerants with long-lasting environmental impacts, such as global warming and ozone depletion [10].

Recently, adsorption technology has been evidenced as the most feasible environmentally friendly alternative for cooling and (or) water desalination systems [11]. This is because it can be driven by low-grade heat sources (50–100 °C), such as solar energy [12–17] or waste heat from engines and industrial processes [18–22]. Therefore, it can reduce the reliance on grid electricity and the accompanying carbon emissions.

* Corresponding authors at: Energy and Bioproducts Research Institute (EBRI), College of Eng. and Physical Science, Aston University, Birmingham, B4 7ET, UK (A. Rezk). Mahmoud B. Elsheniti; Mechanical Engineering Department, College of Engineering, King Saud University, Riyadh 11451, KSA (M. B. Elsheniti).
E-mail addresses: mbadawy.c@ksu.edu.sa (M.B. Elsheniti), a.rezk@aston.ac.uk (A. Rezk).

https://doi.org/10.1016/j.applthermaleng.2023.120642
Received 9 January 2023; Received in revised form 13 April 2023; Accepted 23 April 2023
Available online 27 April 2023

Nomenclature

Symbols

A	Area m^2
A_1	Coefficient in adsorption isotherms equation,kg/kg K
A_2	Coefficient in adsorption isotherms Eq.,kg/kg K^2
A_3	Coefficient in adsorption isotherms Eq.,kg/kg K^3
A_0	Coefficient in adsorption isotherms Eq.,kg/kg
B_1	Coefficient in adsorption isotherms Eq.,K^{-1}
B_2	Coefficient in adsorption isotherms Eq.,K^{-2}
B_3	Coefficient in adsorption isotherms Eq.,K^{-3}
B_0	Coefficient in adsorption isotherms Eq.,K
C_p	Specific heat capacity,J/kg K
CC	Cooling Capacity,kW
COP	Coefficient of performance,—
D_{so}	Pre-exponent constant of surface diffusivity,m^2/s
E_a	The activation energy of surface diffusion,J/kg
k	Thermal conductivity,W/m K
$K_s a_v$	Overall mass transfer coefficient,s^{-1}
K_o	Pre-exponential constant,Pa^{-1}
L	Length,m
$\dot{m}$	Mass flow rate,kg/s
M	Mass,kg
P	Pressure,Pa
$\overline{R}$	Universal gas constant,J/kg K
R_p	Adsorbent particle radius,m
SCP_{mass}	Specific cooling power per unit mass,W/kg_{ads}
SCP_{vol}	Specific cooling power per unit volume,kW/m^3
SDWP	Specific daily water production,$m^3/(ton.day)$
t	Time,s
T	Temperature,K
W	Specific adsorption,kg/kg_{ads}
W_{eq}	Equilibrium adsorption uptake,kg/kg_{ads}

Abbreviations

ADCD	Adsorption cooling cum desalination
HTF	Heat transfer fluid
HTT	Heat transfer tube
MGO	Multi-objective global optimisation
MOF	Metal-organic framework
SG	Silica-gel

Subscripts

ads	Adsorbent
chw	Chilled water
cond	Condenser
cw	Cooling water
evap	Evaporator
Hex	Heat exchanger
hw	Heating water
ref	Refrigerant
sat	Saturation

Greek symbols

ξ, φ, ∂, γ	A group of flags used to enable or disable some of the terms of Eqns. (11) to (13) based on the operating mode
τ	No. of cycles per day

Besides, adsorption systems utilise eco-friendly working fluids like water, methanol, ethanol or ammonia, of a far less environmental impact than other technologies if used for cooling applications [23]. However, adsorption systems still suffer from technical problems that stall their widespread usage [24–26]. For instance, the high heat and mass transfer resistances in the adsorption bed due to the adsorbents' poor thermal performance and mass diffusion lead to heavyweight and sizeable physical footprints [27,28] in conjunction with a low coefficient of performance (COP) and low specific cooling capacity [29]. Many studies have been conducted to overcome such technical problems by improving geometrical and heat & mass transfer by.

- Redesigning the adsorption beds [30–33].
- Optimising the operating parameters of the adsorption cycles [24–26].
- Using different adsorption bed configurations [34,35].
- Enhancing the thermal conductivity inside the adsorption bed using metallic additives [36,37].
- Coating the heating surfaces with the adsorbent material to minimise the thermal contact resistances [38].
- Investigating new adsorbents with high adsorption capacity and stability [39–45].

With the spread of metallic foam production and its remarkable capabilities, coating the adsorbent materials on adsorption beds comprised of metallic foams can considerably boost the system-level thermal performance [46]. Pinheiro et al. [47] proposed a composited coating adsorbent/copper foamed bed using CPO-27(Ni) and AQSOA^{TM} FAM-Z02. Freni et al. [48] proposed a new adsorption bed configuration consisting of highly porous copper foams directly sintered on the external surface of copper pipes and coated with several layers of zeolite 4A by in situ hydrothermal syntheses. This proposed adsorbent bed configuration outperformed the traditional configuration of loose beads or consolidated zeolite in terms of specific and volumetric powers. Mohammed et al. [49] experimentally and computationally investigated the adsorption and desorption processes of the silica gel with different particle sizes packed into an aluminium foamed bed with various pores per inch (PPI) under typical operating conditions for cooling applications.

The emerging metal–organic frameworks (MOFs) that feature high adsorption capacity can replace the classical adsorbent materials and further boost the performance of the adsorption systems side by side with the improvements made in metallic foams. For instance, Furukawa et al. [50] investigated a group of zirconium MOFs based on three criteria: low relative water condensation pressure, high water uptake capacity, and high stability. Among the investigated MOFs, MOF-801 outstood with a water uptake of 22.5 wt% at a relative pressure of 0.1. Moreover, Solovyeva et al. [51] investigated using MOF-801/water for adsorption cooling applications. Under typical adsorption cooling cycle operating conditions, the uptake reached 0.21 kg_w/kg_{ads}.

Kim et al. [52] used MOF-801, applied into copper foam brazed on a copper plate for atmospheric water harvesting, which could produce 2.8 L/kg of MOF-801 at a relative humidity of 20% [52]. Besides, the hydrothermal stability for the dynamic adsorption/desorption behaviour of MOF-801 was confirmed using over 80 cycles in 10,000 min. Kim et al. [53] also used the same method for atmospheric water harvesting in an exceptionally arid climate with relative humidity (10–40%), revealing an uptake of over 0.25 L/kg per cycle. Additionally, copper foam improved the structural stiffness and compensated for the porous adsorbent's poor heat conductivity.

Given the current literature, the effect of operating conditions and geometrical parameters on the performance of the adsorption cooling cum desalination (ADCD) system utilising the state-of-the-art adsorbent MOF-801 with the advanced metal foamed bed is yet to be understood. Therefore, the contribution of this article is to study, for the first time, the influence of the operating conditions and the physical parameters on the overall ADCD system utilising MOF-801 packed into a copper foamed adsorbent bed. Besides, the multi-objective global optimisation,

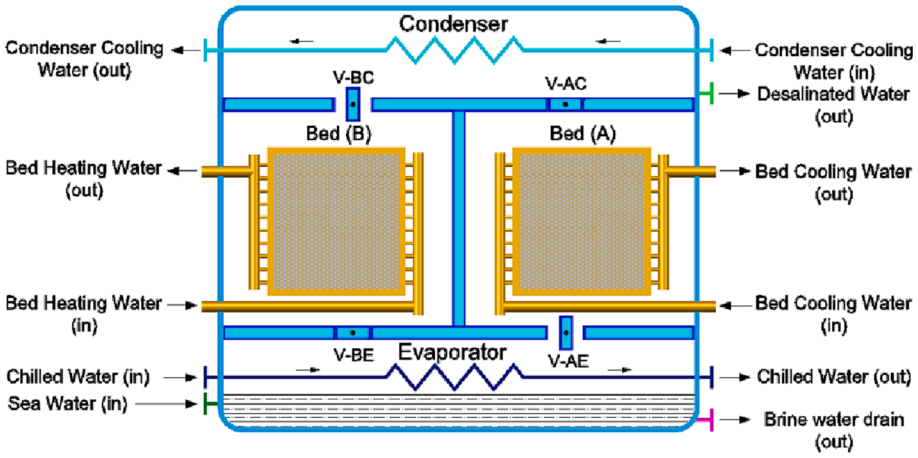

Fig. 1. Schematic diagram for the simulated adsorption system.

Table 1
Operation modes and valve positioning.

Operation Modes	Bed (A)	Bed (B)	AE	AC	BE	BC
Mode (1)	Precooling	Preheating	X	X	X	X
Mode (2)	Cooling/Ads	Heating/Des	O	X	X	O
Mode (3)	Preheating	Precooling	X	X	X	X
Mode (4)	Heating/Des	Cooling/Ads	X	O	O	X

employing in MATLAB platform, was utilised to identify the optimal operating conditions aiming for the maximum specific cooling power simultaneously with the maximum coefficient of performance. Accordingly, three tasks were undertaken to enable the optimisation study and understand its results: ***(1)*** developing a novel one-dimensional thermal resistance model for a foamed bed sintered with MOF-801; ***(2)*** coupling the developed adsorbent bed model with a previously validated empirical lumped analytical model for ADCD; ***(3)*** developing the fundamental understanding of the influence of operating and physical parameters on the overall system's performance.

2. System description

Fig. 1 shows a schematic diagram for the simulated two-bed adsorption system for water desalination cum cooling. Each adsorbent bed is connected to the evaporator by valves VA-E and V-BE during adsorption/evaporation or condenser by valves VA-C and V-BC during desorption/condensation. The valves are closed during preheating/precooling modes to develop sufficient pressure difference required for the water vapour mobility between the bed and the connected evaporator or condenser. Accordingly, the operation modes and valve opening are shown in Table 1, as (X) symbolises a closed valve and (O) symbolises an opened valve.

The adsorbent bed heat exchanger is constructed from copper foamed tubes packed with the adsorbent granules, as shown in Fig. 2. In this study, MOF-801 was employed and benchmarked against silica-gel baseline adsorbent. Table 2 shows the thermophysical properties of MOF-801 and silica-gel and the physical dimensions of the adsorbent beds. Table 3 shows the physical and geometrical data for the evaporator and condenser. Finally, Table 4 shows the nominal operating parameters for the basic model.

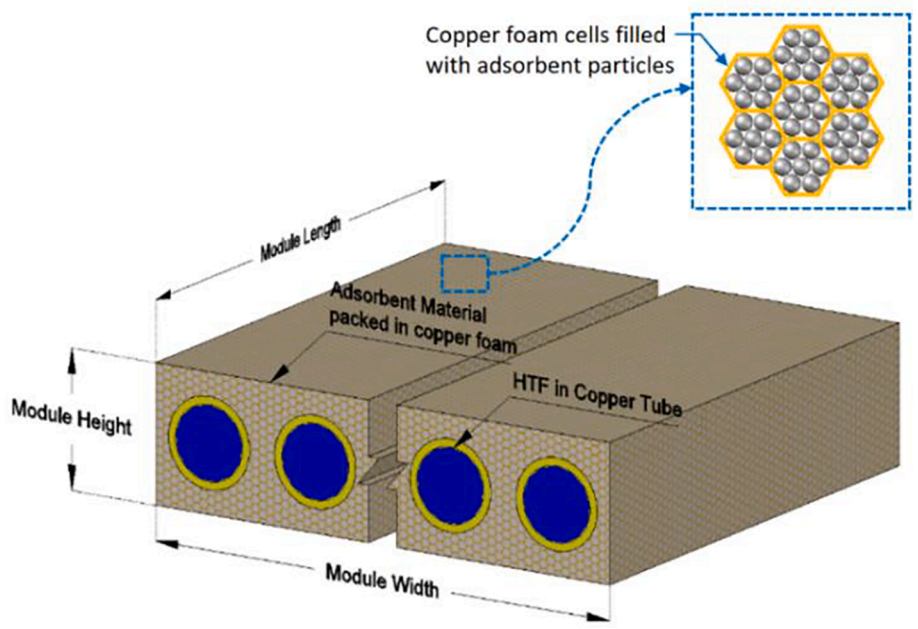

Fig. 2. Copper foam bed packed with adsorbent material with detailed copper foam cells filled with adsorbent particles.

Table 2
Physical and geometrical characteristics of the adsorption bed.

Parameter	Symbol	Value	
Physical properties of the adsorbent materials		MOF-801	Silica-gel
Average particle diameter (m)	d_p	$1x10^{-6}$	$0.32 x10^{-3}$
Particle density (kg/m^3)	ρ_p	1400	2027
Packing bed density (kg/m^3)	ρ_b	464	691
Specific heat of adsorbent (J/kg.K)	$C_{p,ads}$	760	921
Heat of adsorption (J/kg)	ΔH_{ads}	$3.053 x10^6$	$2.510 x10^6$
Bulk bed thermal conductivity (W/m.K)	k_{bed}	3	
Copper foam porosity (%)	ε_{foam}	95	
Specific heat of copper foam (J/kg.K)	$C_{p,foam}$	390	
Geometric parameters of the adsorption bed			
No. of modules	N_m	16 per bed	
Module length (mm)	L_m	1000	
Module width (mm)	W_m	340	
Module height (mm)	H_m	VAR (20–24-28–32) mm	
Heat transfer tube			
HTT material		Bare copper tube	
HTT material density (kg/m^3)	$\rho_{bed,t}$	8100	
HTT material specific heat (J/kg.K)	$C_{p,bed,t}$	383	
HTT thermal conductivity (W/m.K)	$k_{bed,t}$	310	
HTT length (mm)	$L_{bed,t}$	1000	
HTT outer diameter (mm)	$d_{bed,t,o}$	15.875	
HTT inner diameter (mm)	$d_{bed,t,i}$	14.275	
Number of HTT	$N_{m,t}$	12 per module	

Table 3
Physical and geometrical characteristics for the evaporator and condenser.

Parameter	Symbol	Value
Evaporator		
HTT material		Externally enhanced copper tube
HTT material density (kg/m^3)	$\rho_{evap,t}$	8100
HTT material specific heat (J/kg.K)	$C_{p,evap,t}$	383
HTT thermal conductivity (W/m.K)	$k_{evap,t}$	310
HTT length (mm)	$L_{evap,t}$	26,000
HTT outer diameter (mm)	$d_{evap,t,o}$	10
HTT inner diameter (mm)	$d_{evap,t,i}$	9
Number of passes	$N_{evap,pass}$	1
Number of HTT	$N_{evap,t}$	6
Condenser		
HTT material		Bare copper tube
HTT material density (kg/m^3)	$\rho_{cond,t}$	8100
HTT material specific heat (J/kg.K)	$C_{p,cond,t}$	383
HTT thermal conductivity (W/m.K)	$k_{cond,t}$	310
HTT length (mm)	$L_{cond,t}$	950
HTT outside diameter (mm)	$d_{cond,t,o}$	12.7
HTT wall thickness (mm)	$d_{cond,t,i}$	11.1
Number of passes	$N_{cond,pass}$	4
Number of HTT	$N_{cond,t}$	72

3. Methodology

This section presents the computational modelling of the ADCD system. Firstly, the sorption properties of the investigated material (adsorption isotherm and kinetics) were modelled. Next, the sorption and heat transfer properties were employed to simulate the ADCD system components: adsorption bed, evaporator, and condenser. Finally, the models of the components were integrated to form the overall system model.

3.1. Adsorption isotherm modelling

Adsorption isotherms determine the equilibrium water uptake at a given pressure ratio between the interconnected heat exchange (i.e., the evaporator and the condenser) and the adsorbent bed at a given adsorption/desorption temperature. The experimentally developed adsorption isotherms for MOF-801 by Kim et al. [53] at temperatures 25 °C – 85 °C showed s-shaped isotherms. Different models can replicate such isotherms, e.g., the Do-Do model [54] and utilise a group of exponential and polynomial equations [55]. In this study, the adsorption isotherms were modelled using a group of exponential and polynomial equations (1) – (3), which was deemed more suitable for the investigated case. The choice between the exponential and polynomial forms depends primarily on the pressure ratio. It is noteworthy that modelling the isotherms based on the experimental data within the above-mentioned ranges is acceptable to extrapolate the adsorption properties for the extended temperature range [55,56].

Table 4
Operation parameters for the basic model.

Property	Value
Adsorption bed reactor	
$\dot{m}_{bed,cw}$	7.42 kg/s
$\dot{m}_{bed,hw}$	3.36 kg/s
$T_{bed,cw,i}$	30° C
$T_{bed,hw,i}$	85° C
$t_{preheat}$-$t_{precool}$	40 sec
t_{cyc}	VAR (200–1000) sec
Bed initial temp.$T_{bed,init}$	30° C
Condenser	
$\dot{m}_{cond,cw}$	7.42 kg/s
$T_{cond,cw,i}$	30° C
Condenser initial temp.$T_{cond,init}$	30° C
Evaporator	
$\dot{m}_{evap,chw}$	0.90 kg/s
$T_{chw,i}$	15° C
Evaporator initial temp.$T_{evap,init}$	30 °C

Table 5
Modified Freundlich equation constants for RD-Silica gel/water adsorption isotherms [58,59].

Constant	Value	Unit	Constant	Value	Unit
A_0	−6.5314	Kg/kg K	B_0	−15.587	K
A_1	0.72452E-1	Kg/kg K	B_1	0.15915	K^{-1}
A_2	−0.23951E-3	Kg/kg K^2	B_2	−0.50612E-3	K^{-2}
A_3	0.25493E-6	Kg/kg K^3	B_3	0.53290E-6	K^{-3}

$$w^* = 2.18865 * exp(-6.61855669E-4A)(A > 6200) \quad (1)$$

$$w^* = 7.6163E-11A^3 - 1.240E-6A^2 + 6.5914E-3A - 11.297 (6200 \geq A \geq 4900) \quad (2)$$

$$w^* = -1.763E-16A^4 - 1.2384E-12A^3 + 2.2088E-8A^2 - 1.0597E-4A + 0.419 (A < 4900) \quad (3)$$

Where w* is the uptake value at equilibrium conditions and A is the adsorption potential Equation (4).

$$A = \overline{R}Tln\left(\frac{p}{p_{ads}}\right)(0.002(T-318)) + 1) \quad (4)$$

Where $\overline{R}$ is the universal gas constant; T is the temperature of the adsorbent material; (p/p_{ads}) is the evaporator-to-bed pressure ratio during the adsorption process or condenser-to-bed pressure ratio during the desorption process.

Silica gel/water isotherms show type-I. Different models can replicate such isotherms, e.g., Langmuir [57] and Modified Freundlich [58,59]. In this study, the Modified Freundlich model was employed to

Table 6
The linear driving force, LDF equation constants.

Symbol	MOF-801 (This work)	Silica gel [58]	Unit
FD_{so}	$1.30558x10^{-10}$	3.81×10^{-3}	m/s^2
E_a	$3.1533x10^{4}$	4.2×10^{4}	J/mol
R_p	$5x10^{-7}$	0.16×10^{-3}	m
k_0	522.23	1.488×10^{5}	s^{-1}
$k_s a_v$*	1.55×10^{-3}	6.46×10^{-3}	–

*The value was determined at a mean temperature 25 °C

replicate the adsorption isotherms for RD-Silica gel/water, as shown in the equations (5) - (7). The numerical values of A_0-A_3 and B_0-B_3 are furnished in Table 5.

$$w^* = A(T_{ads})\left[\frac{P_{sat(T_{ref})}}{P_{sat(T_{ads})}}\right]^{B(T_{ads})} \tag{5}$$

$$A(T_{ads}) = A_0 + A_1 T_{ads} + A_2 T_{ads}^2 + A_3 T_{ads}^3 \tag{6}$$

$$B(T_{ads}) = B_0 + B_1 T_{ads} + B_2 T_{ads}^2 + B_3 T_{ads}^3 \tag{7}$$

3.2. Adsorption kinetics modelling

The Linear Driving Force model (LDF) was employed to determine the adsorption uptake in the time frame of reference for MOF-801 and RD silica gel for water adsorption, as shown in Equations (8) - (10)[26].

$$\frac{dw}{dt} = k_s a_v (w^* - w) \tag{8}$$

Where, $k_s a_v$ is the overall intra-particle mass transfer coefficient for the adsorption/desorption process, which is a function of the activation energy E_a and adsorption temperature, as shown in Equation (9) [60].

$$k_s a_v = k_0 exp\left(\frac{-E_a}{\bar{R}T}\right) \tag{9}$$

$$k_0 = \frac{F.D_{so}}{R_p^2} \tag{10}$$

Where k_0 is the (LDF) model empirical constant comprises the geometry constant (F) that equals 15 for the spherical adsorbent particles, the pre-exponent constant (D_{so}) and the average radius of the adsorbent particle (R_p). The (LDF) equation constants are furnished in Table 6. Such a level of material characterisation was previously used by Elsayed et al. [55], which was suitable for adsorption beds and overall system modelling.

3.3. Adsorption system modelling

The ADCD system was simulated using an empirical lumped analytical model (ELAM) approach. A computational solver employing MATLAB computational modelling platform was developed. The solver determined the variation of thermophysical properties of the working fluids with varying operating conditions (i.e., temperatures and pressures) by coupling the REFPROP database. Fig. 3 shows the modelling flow chart of the simulated system. The model encompasses three submodels that simulate the heat and mass transfer during the adsorption/desorption and precooling/preheating processes in the adsorption bed(s), condenser and evaporator. The model accounted for the variation of the overall heat transfer coefficient of the heat exchangers influenced by the variation of the thermophysical properties of the working fluids due to dynamic (i.e., time-dependent) temperature variation. Besides, the assumptions below were employed.

- Constant bulk thermal conductivity (3 W/m.K) for the copper-packed foam using MOF-801 and silica gel, as reported by Kim et al. [53].
- The effect of saline water on the evaporator cooling power was neglected.
- The adsorbent, water vapour adsorbate and heat exchanger metal are assumed to be momentarily at the same temperature (i.e., momentarily lumped).
- The system is insulated from the surroundings (i.e., the heat exchange with the ambient is neglected).

Equations (11) - (14) govern the dynamic energy and mass transfer for adsorption beds, the evaporator, and the condenser [61].

$$\left(\xi M_{w,ads} Cp_w(T_{bed}) + M_{ads} w_{bed} Cp_w(T_{bed}) + M_{ads} Cp_{ads} + M_{Hex,bed} Cp_{Hex,bed}\right)\frac{dT_{bed}}{dt} =$$

$$(\varphi.\partial) M_{ads}\frac{dw_{bed}}{dt}\left[\gamma\left\{h_g(T_{Hex}) - h_g(P_{Hex}, T_{bed})\right\} + (1-\gamma)\left\{h_g(P_{Hex}, T_{bed}) - h_g(P_{bed}, T_{bed})\right\}\right] +$$

$$\varphi M_{ads}\frac{dw_{bed}}{dt}\Delta H_{ads} + (1-\xi)\sum_{n=1}^{n=N_{bed}} dUA_{bed,k} \times LMTD_{bed} \tag{11}$$

$$\left[Cp_{w,l}(T_{evap}) M_{w,evap} + Cp_{Hex,evap} M_{Hex,evap}\right]\frac{dT_{evap}}{dt} = UA_{evap} \times LMTD_{evap} +$$

$$\varphi M_{ads}\frac{dw_{bed}}{dt}\left[h_{w,evap,in} - h_{w,evap,out}\right] + \frac{dE_{pump}}{dt} \tag{12}$$

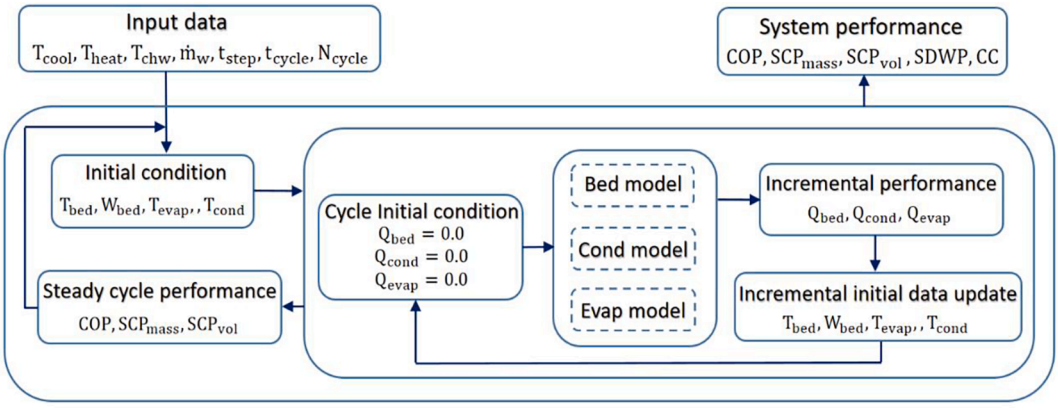

Fig. 3. System modelling flow chart.

Table 7
Simulation model switching flags.

Mode	Flag ξ	Flag φ	Flag ∂	Flag γ
ads - evaporation	0	1	1	1
des - condensation	0	1	0	0
Mass recovery	1	0	1	0
Heat recovery	0	0	1	0

$$\left[Cp_{w,l}(T_{cond})M_{w,cond}+M_{Hex,cond}Cp_{Hex,cond}\right]\frac{dT_{cond}}{dt}=UA_{cond}\times LMTD_{cond}+$$

$$\varphi M_{ads}\frac{dw_{bed}}{dt}\left[\left(h_{w,cond}-h_{w,cond,g}\right)+Cp_{ads}(T_{cond}-T_{bed})\right] \quad (13)$$

$$\frac{dM_{w,f,evap}}{dt}=-\varphi.M_{ads}\left(\frac{dw_{des}}{dt}+\frac{dw_{ads}}{dt}\right) \quad (14)$$

Where M, C_p, T, LMTD, P, h, w, H_{ads} and t are the mass, specific heat at constant pressure, temperature, log mean temperature difference, pressure, specific enthalpy, uptake value, isosteric heat of adsorption, and time, respectively. The subscripts bed, evap and cond denote adsorbent bed, evaporator and condenser, respectively. Subscripts HTF, ads and w denote the heat transfer fluid (i.e., cooling and heating water), adsorbent, and water vapour (i.e., adsorbate). Subscripts g and f denote the saturated vapour and liquid condition, and Hex denotes the heat exchanger that interconnects with the adsorbent bed. As shown in Table 7, a group of flags (ξ, φ, ∂ and γ) were used to enable or disable the equation's terms based on the operating mode.

The overall heat transfer coefficients U for the heat exchangers, including the adsorbent bed, were determined based on the fundamental heat transfer equations. There are five heat transfer resistances: forced convection thermal resistance between heat transfer fluid and internal tube wall (R1); conduction thermal resistance through tube wall (R2); contact thermal resistance between the tube outside surface and adsorbent packed foam (R3); thermal conduction resistances through adsorbent packed foam radial direction (R4); and thermal conduction resistances through adsorbent packed foam axial direction (R5). As such, the overall heat transfer network for the segmental copper foamed adsorbent bed control volume is shown in Fig. 4. Each segment comprises a copper tube surrounded by copper foam packed with the adsorbent material. Equations (15) - (19) correlate the heat transfer resistances to the segment dimension and material properties.

(a) the water side heat transfer resistance ($R_{w,bed}$)

$$R_1=1/(htc_iA_i) \quad (15)$$

(b) the tube wall heat transfer resistance ($R_{t,bed}$)

$$R_2=\left[ln(d_{p,o}-d_{p,i})\right]/(2\pi k_tL) \quad (16)$$

(c) the outside surface heat transfer resistance ($R_{o,bed}$)

$$R_3=R_{cont}/(\pi d_oL) \quad (17)$$

$$R_4=\left[ln(d_{ads}/d_{p,o})\right]/(2\pi k_{ads}L) \quad (18)$$

$$R_5=(L/2)/(A_{ads}k_{ads}) \quad (19)$$

Where htc, A_i, A_{ads}, $d_{p,i}$, $d_{p,o}$, k, R_{cont} and L are the forced convection heat transfer coefficient, tube internal surface area, equivalent surface area for the packed foamed bed, inner pipe diameter, outer pipe diameter, thermal conductivity, contact thermal resistance and the axial segment length, respectively. The overall incremental heat transfer conductance dUA_{bed} was then written as equation (20).

$$dUA_{bed}=\frac{1}{R_{w,bed}+R_{t,bed}+R_{o,bed}} \quad (20)$$

In the evaporator and condenser components, there are three heat transfer resistances connected in series: forced convection heat transfer between the heat transfer fluid and internal tube wall, conduction heat transfer resistance in the copper tube wall, and convection heat transfer resistance between the water vapour and external tube surface during desorption/condensation or adsorption/evaporation.

3.4. Performance indicators

The cyclic cooling capacity (Q_{evap}), heating power (Q_{cond}), specific cooling power per unit mass (SCP_{mass}) and per unit volume (SCP_{vol}), coefficient of performance (COP) and specific daily water production (SDWP) are determined using Equations (20)-(25).

$$Q_{evap}=\int_0^{t_{cycle}}\dot{m}_{chw}Cp_{chw}(T_{chw,in}-T_{chw,out})dt/t_{cyc} \quad (21)$$

$$Q_{cond}=\int_0^{t_{cycle}}\dot{m}_{hw}Cp_{hw}(T_{hw,in}-T_{hw,out})dt/t_{cyc} \quad (22)$$

$$SCP_{mass}=\frac{Q_{evap}}{M_{ads}} \quad (23)$$

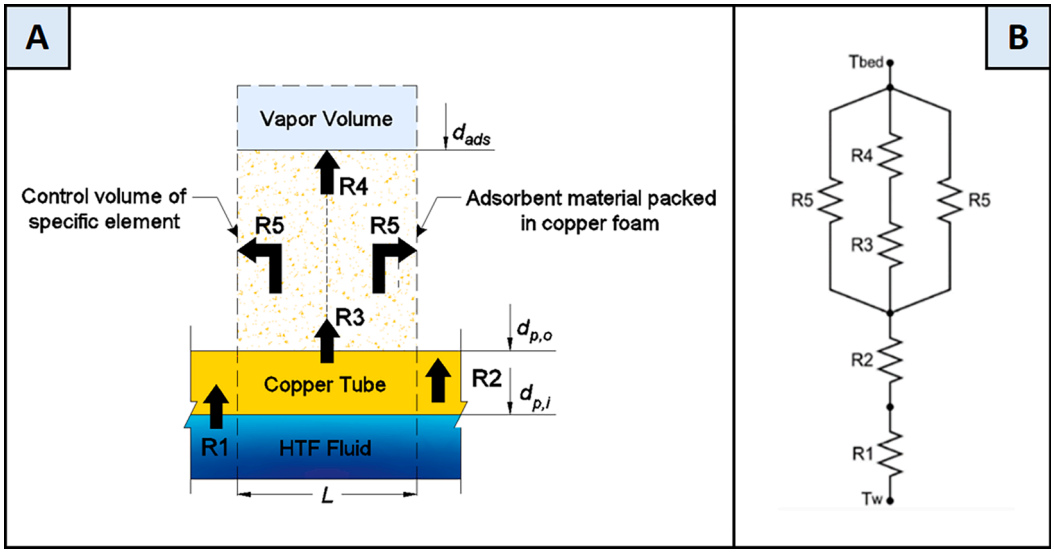

Fig. 4. (A) Control volume of an element in the adsorber bed, (B) Heat transfer resistance schematic diagram.

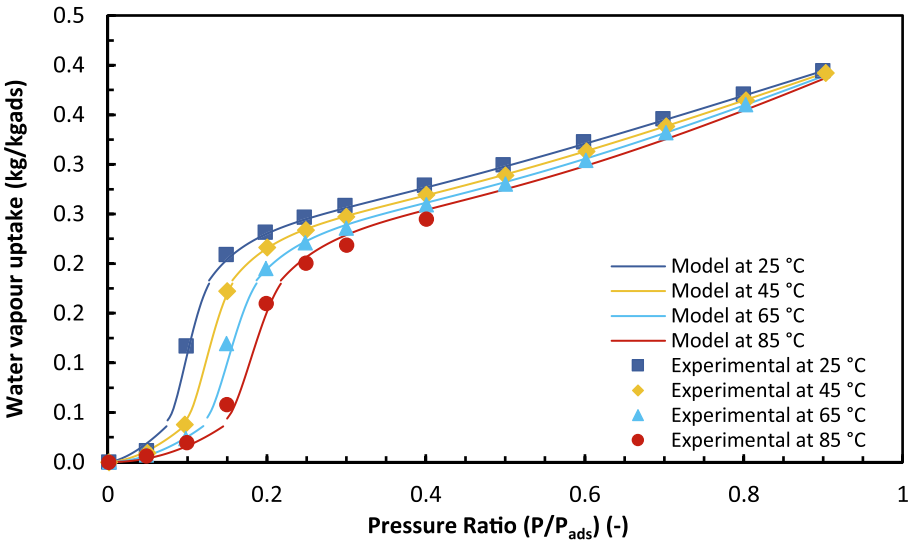

Fig. 5. Validation of the proposed fitting isotherm model with the experimental data [53].

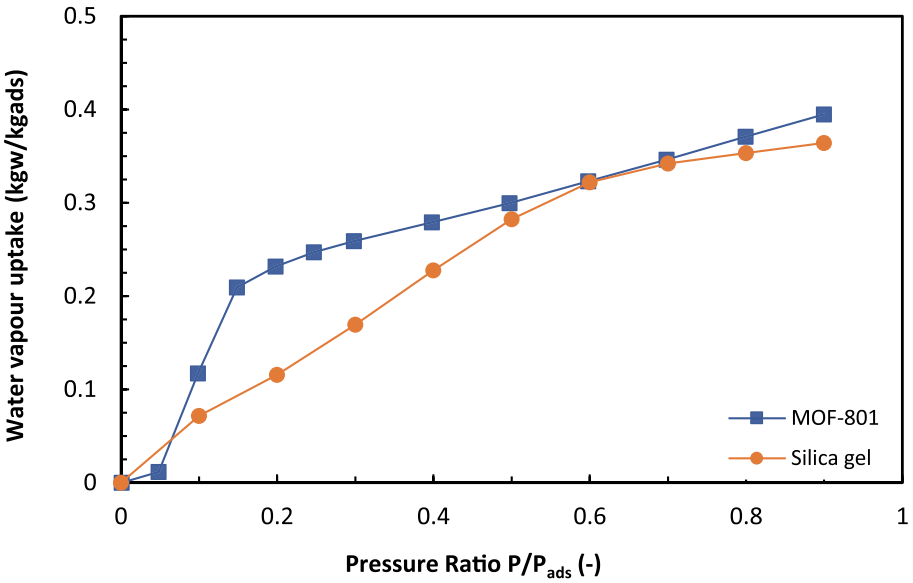

Fig. 6. Comparison between MOF-801 and silica gel isotherms.

$$SCP_{vol} = \frac{Q_{evap}}{V_{ads}} \tag{24}$$

$$COP = \frac{Q_{evap}}{Q_{cond}} \tag{25}$$

$$SDWP = \int_0^{t_{cycle}} \frac{Q_{cond} \bullet \tau}{h_{fg} M_{ads}} dt \tag{26}$$

Where Q, $\dot{m}$, Cp, T, t, M, V and h are heat, flow rate, specific heat at constant pressure, temperature, time, mass, volume and specific enthalpy. Subscripts chw, hw, in, out, cyc, ads, f, and g denote the chilled water, heating water, inlet, outlet, cycle, adsorbent, fluid and gas, respectively.

4. Results and discussions

4.1. Adsorption isotherm validation

A good agreement between the experimental and modelled isotherms was observed, as shown in Fig. 5.

Fig. 6 shows the experimental adsorption isotherms for both MOF-801 and silica gel RD2060 at 25 °C. According to the IUPAC classification, MOF-801/water isotherm can be classified as type V, while silica gel/water isotherm can be classified as type I.

4.2. Adsorption kinetics validation

A good agreement between the predicted kinetic and measured uptake curves for MOF-801 was observed, as shown in Fig. 7.

4.3. Adsorption system validation

The validity of the developed numerical solver was undertaken by benchmarking the temporal bed temperature and water vapour uptake for the simulated bed during adsorption and desorption against the equivalent experimental values published by Mohammed et al. [49], as shown in Fig. 8. In addition, the validation was undertaken for the same geometry and adsorbent material (i.e., silica gel), the baseline material

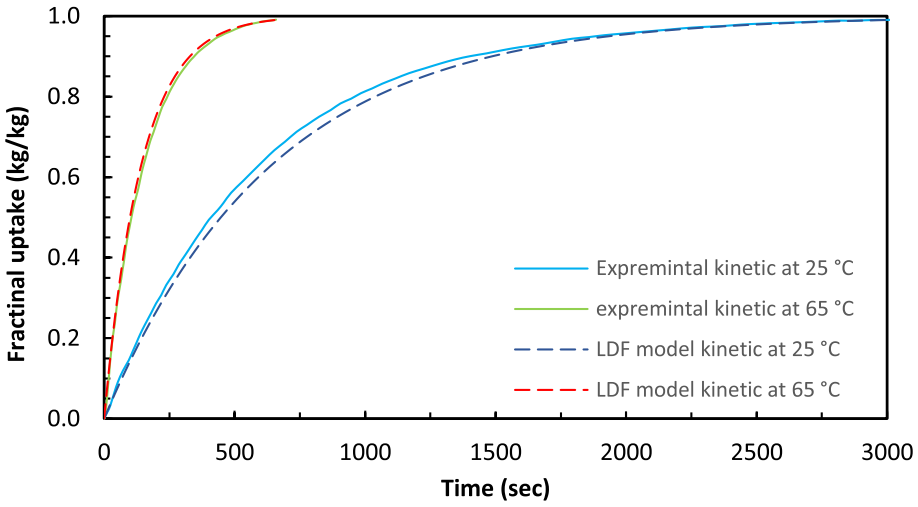

Fig. 7. Validation of the proposed (LDF) kinetic parameters for MOF-801 with the measured uptake curves at a partial pressure of 25% [53].

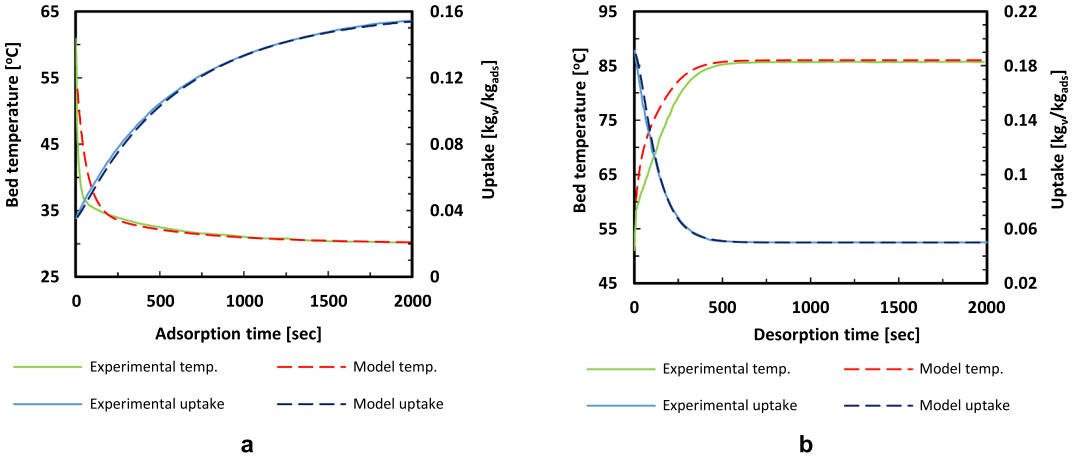

Fig. 8. Model validation for the average temperature and uptake of silica gel/aluminium foam model using the present model in this study and those experimental data corresponding in reference [49] (a) during adsorption and (b) during desorption.

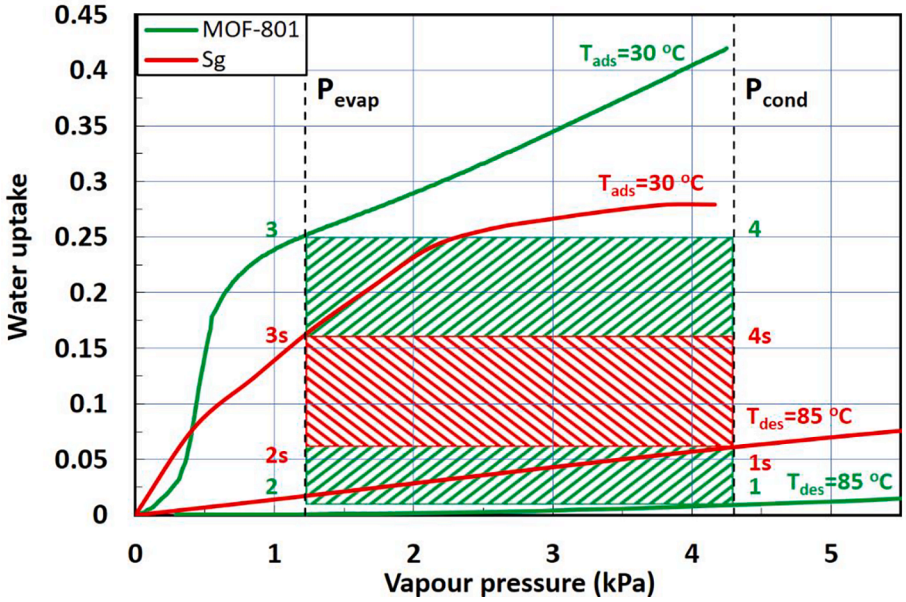

Fig. 9. MOF-801 and silica gel cyclic uptake potential.

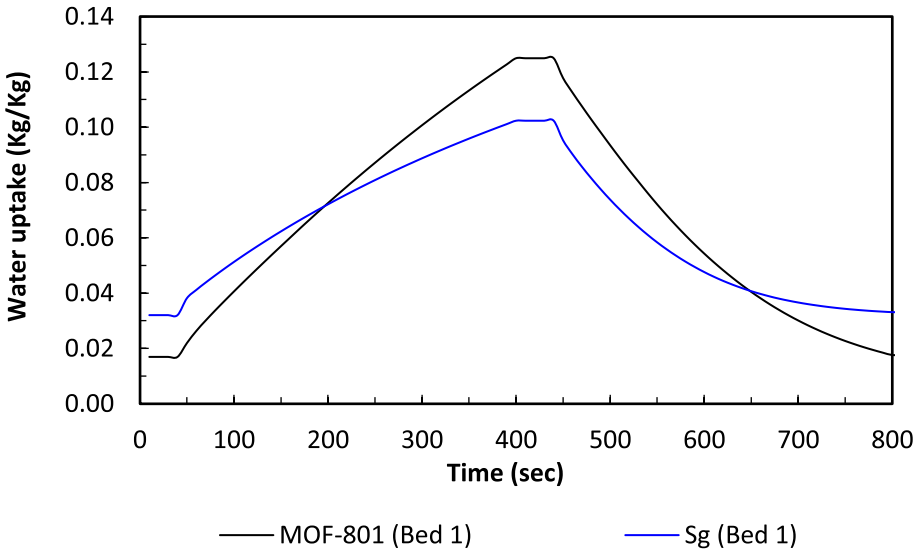

Fig. 10. The uptake-time profile for MOF-801 and silica gel at cycle time 400 s and bed height 24 mm.

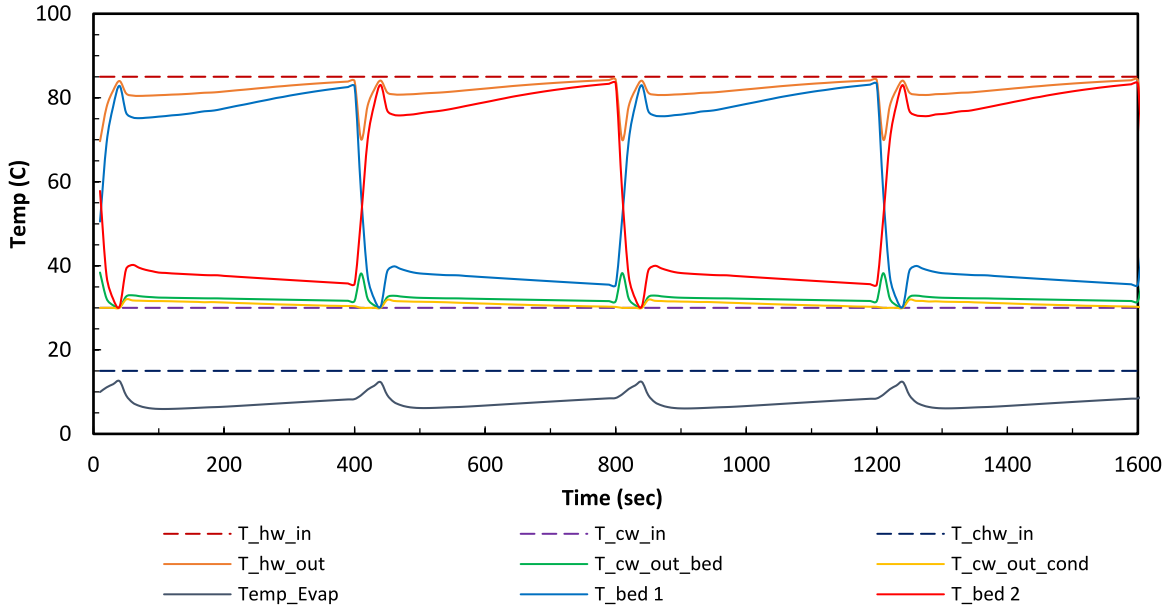

Fig. 11. Temperature-time profile for MOF-801 at cycle time 400 s and bed height 24 mm.

for the current study. As a result, good agreement between the numerical and experimental data was observed, indicating the suitability of this model to simulate the heat and mass transfer inside a packed foamed adsorbent bed. Besides, the validation of the overall adsorption system numerical solver was examined in previously published work by Rezk et al. [61,62]. Besides, the solver was employed and showed a high level of reliability by Elsheniti et al. [63].

4.4. Cyclic water uptake and kinetics

Fig. 9 shows the cyclic equilibrium uptake of MOF-801 and silica gel at the material level for adsorption, evaporation, desorption, and condensation temperatures of 30 °C, 15 °C, 85 °C and 30 °C. The cycle time was 400 s, including a 40 sec switching time, and the bed height was 24 mm. It can be observed that the cyclic uptake of MOF-801 outperforms that of silica gel by 150%, as the cyclic uptake was 0.25 kg_w/kg_{ads} for MOF-801 and 0.1 kg_w/kg_{ads} for silica gel for the given operating temperatures. At the component (i.e., adsorbent bed) level, the enhanced adsorption performance of MOF-801 led to a 54% increase in the overall cyclic uptake compared to silica gel, as shown in Fig. 10.

As shown in equation 8, the adsorption/desorption rate is a function of the intra-particle mass transfer determined by $k_s a_v$ and the equilibrium uptake (w^*). Arithmetically, the equilibrium uptake dominates the rate of adsorption/desorption due to its higher order of magnitude. Therefore, the overall cyclic enhancement at the component level is primarily attributed to the enhanced equilibrium uptake of MOF-801, specifically at low-pressure ratios (pressure ratio less than 0.3) that replicate the actual operating conditions. It intensified the amount of water vapour uptake/offtake for the given cycle time for MOF-801 by 158% compared to that for silica gel. It is noteworthy that although the implication of the adsorbent material's thermal conductivity was overlooked, as per the numerical modelling assumptions, the lower specific heat of MOF-801 contributed to enhancing the thermal response of the adsorbent bed thus promoting the adsorption/desorption kinetics.

Figs. 11 and 12 show the dynamic temperature profiles for MOF-801 and silica gel, respectively. These profiles manifest the implication of a

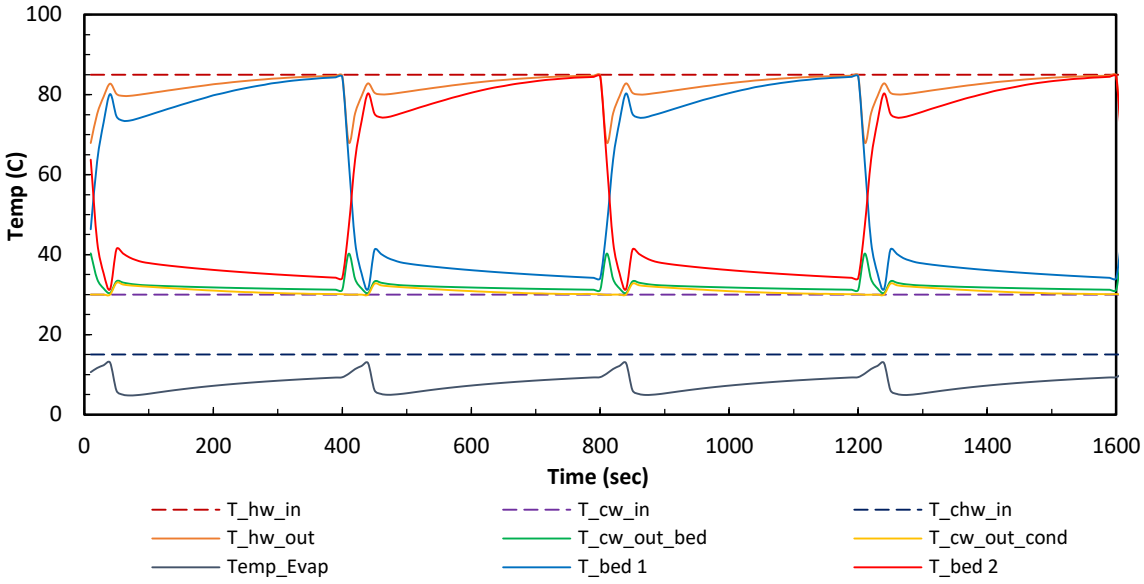

Fig. 12. Temperature-time profile for silica gel at cycle time 400 s and bed height 24 mm.

slower thermal response of MOF-801 packed bed due to its higher overall heat capacity than a silica gel one. Although MOF-801 has lower specific heat than silica gel at the material level, the packing density of the former is 32.8% lower than the latter, which led to an overall higher heat capacity of MOF-801 packed bed to be dominated by the copper foam at the component level. The higher heat capacity of the adsorbent bed led to larger heat stored during the desorption mode, consequently slower cooling during the adsorption mode and eventually lower COP at the system level. For example, the COP for the MOF-801-based system was 3.6% lower than that for the SG-based system. The compound effect of cyclic water uptake and thermal response led to a higher cyclic cooling capacity for the MOF-801-based system by 4.8% than the SG-based system.

4.5. *The effect of the cycle time.*

Fig. 13 shows the influence of varying the cycle time (from 200 to 1000) and bed height (from 20 to 32 mm) on the overall system performance for MOF-801 and silica gel-packed foamed bed. Notably, the investigated bed height range is broad enough to provide a wide spectrum of results to conclude its impact on the system performance. Besides, although the cycle time might be fixed for a specified application area, i.e., practical installation, it is crucial to develop insight into its impact on the system performance, which will vary from one application to another. It can be observed that within the investigated range, SDWP, SCP_{mass} and SCP_{vol} for MOF-801 packed bed slightly increased, peaked at 300 s, and then gradually decreased by increasing the cycle time. The cooling capacity for MOF-801 packed foamed bed followed the same trends but peaked at 400 s for 28–32 mm foam height. Compared to silica gel, SDWP, CC, SCP_{mass} and SCP_{vol} packed foam heights of 24–32 mm remained nearly constant at 200 and 300 s, then gradually decreased by increasing the cycle time. Although increasing the cycle time leads to higher quantities of water vapour adsorption, the adsorption rate decreases closer to the saturation conditions, reducing the cyclic rate of cooling and water production. Such phenomenon elucidates the variation of SDWP, SCP_{mass} and SCP_{vol} trends with varying cycle times. For 20 mm height SG-packed bed foam, SDWP, SCP_{mass} and SCP_{vol} decreased by increasing the cycle time, owing to the low packed adsorbent mass.

The advanced adsorption characteristics of MOF-801 led to a notable increase in SDWP, SCP_{mass} and CC over those for SG-packed bed for the exact bed heights, but the difference in CC between MOF-801- and SG-based systems are close. Moreover, SCP_{vol} for SG-based system outperformed that for MOF-801 below 400 s at 20 mm height and below 300 s at 24 mm height. The difference between CCs at 28 and 32 mm below 300 s is marginal but slightly higher in the MOF-801-based system. The contradicting trends at short cycle time for SCP_{vol} is attributed to the lower packed density of MOF-801 (464 kg/m^3) compared to silica gel (691 kg/m^3). The difference in the packing densities led to, for example, 31.2 kg MOF-801 compared to 46.5 kg SG-packed bed masses into 20 mm foamed height. Such differences in SCP_{vol}, despite the advanced adsorption characteristics of MOF-801, its low density negates such advances, in terms of physical footprint, at short cycle times simultaneously with small foam height.

Fig. 14 shows the overall thermal masses of the adsorbent beds and the contribution of the metal and adsorbents utilised at different heights. The thermal mass contribution of the metal affects the COP as more heat is stored in the bed's metal. The higher the thermal mass of the metal, the longer it takes to cool it during the adsorption process, which subsequently reduces the COP of the system at a given time. It is manifested by the relatively higher COP of SG-packed bed than MOF-801 counterpart at longer cycle times, owing to the larger contribution of the adsorbent's thermal mass. As a result, the mean COP difference between MOF-801- and SG-packed bed at 300 sec was lower than that at 1000 sec by 623.2% (0.008–0.056). On the other hand, the mean COP for MOF-801-packed bed is higher than that for SG-packed bed by 2% at 200 sec, emphasising the benefit of utilising MOF-801 but at short cycle time and small fin height to better utilise its advanced adsorption characteristics.

Changing the foam height showed a crucial influence on the overall system performance. On the one hand, increasing the foam height led to more absolute adsorbent-packed masses, consequently increasing the cyclic cooling capacity. On the other hand, increasing the foam height increases the thermal mass of the adsorbent bed owing to the higher compound specific heat of copper and the adsorbent, affecting the overall COP at the cycle level, even though the increased copper foam enhances the overall thermal conductance. The combined contradicting trends of COP and CC resulting from increasing the foam height led to reducing the SCP and SDWP by increasing the foam height. This leads to the conclusion that low foam height persists better initial cost-effectiveness with negligible effect on the energy conversion efficiency measured by COP in the case of MOF-801 compared to a more notable change in COP in SG-packed bed foam, yet more efficient than MOF-801 in the case of longer cycle time.

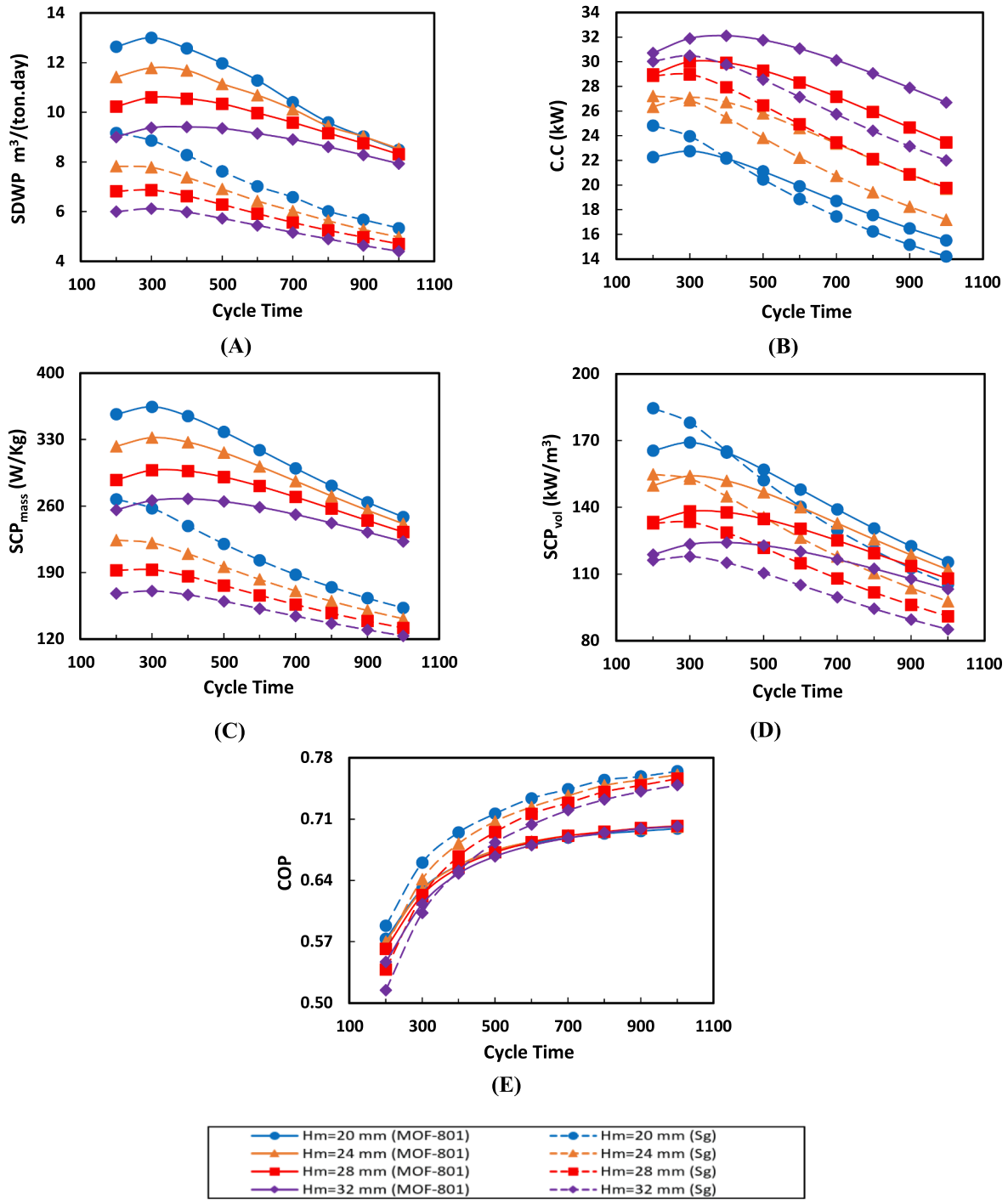

Fig. 13. The effect of the cycle time and bed height on A-SDWP, B-CC, C-SCPmass, D-SCPvol and COP.

4.6. The effect of heat source temperature

Fig. 15 shows the influence of the heating water inlet temperature (from 70 °C to 90 °C) and bed height (from 20 to 32 mm) on the system performance for MOF-801 benchmarked against SG-packed bed foamed bed. The cycle time, cooling water inlet temperature, and chilled water inlet temperature was maintained at 400 s, 30 °C and 15 °C, respectively.

Generally, increasing the heating water inlet temperature increases the desorbed adsorbate, promoting the adsorbed water vapour, specifically at the early stages of the adsorption modes [65]. Building on this fact, increasing the heating water inlet temperature from 70 °C to 90 °C gradually increased the SDWP and SCP$_{mass}$ of MOF-80- and SG-based systems. Given the advanced adsorption characteristics of MOF-801, it enhanced the system's SDWP and SCP$_{mass}$ compared to the silica-gel over the investigated range of temperatures and foam heights. It was observed that the SDWP and SCP$_{mass}$ increased between 70 and 80, steeper than that from 80 to 90 for MOF-801. However, it increased more gradually in the case of silica gel. Such differences in SDWP and SCP$_{mass}$ increments are attributed to the consistent increase in the equilibrium uptake for silica gel at the material level, unlike the inconsistent isotherm profile for MOF-801 at small relative pressures (below 0.2) corresponding to the desorption/condensation process, which is slower than silica gel. The maximum observed increment for

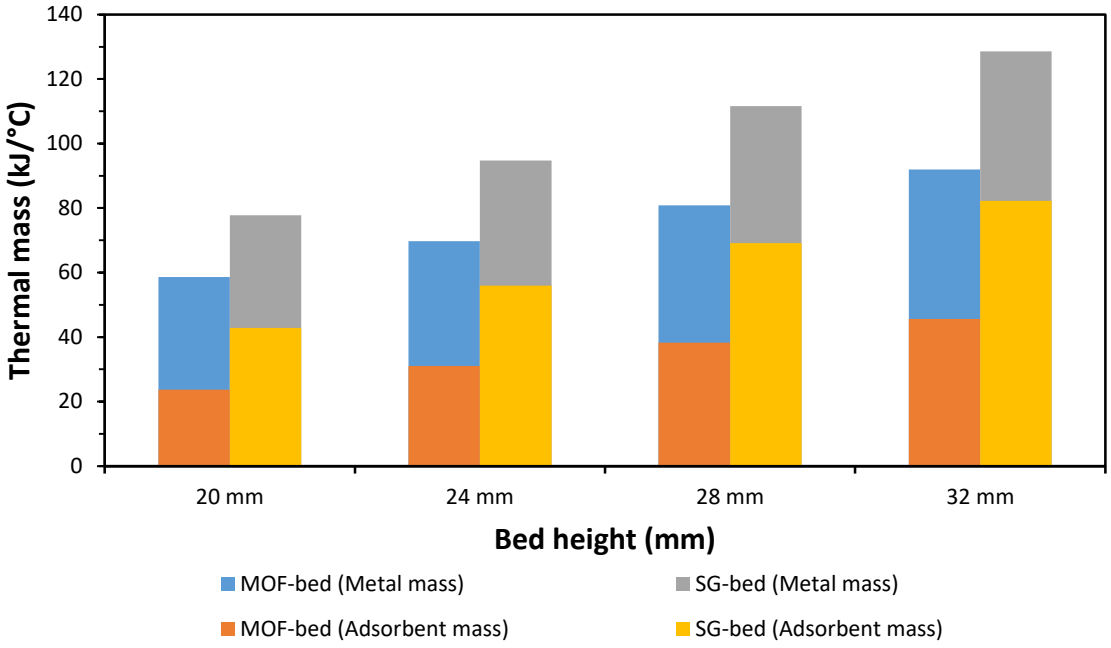

Fig. 14. The thermal masses of the adsorbent bed and their components.

MOF-801 occurred by increasing the heating temperature from 70 °C to 80 °C was 77% compared to 24% for silica-gel at 20 mm bed height.

Although increasing the heat source temperature promotes the cooling capacity, it increases the temperature, i.e., grade, of heat stored in the adsorbent bed; lower heat sink temperatures might be required for a given cycle time to combat such stored heat. Therefore, by increasing the heat source temperature, the COP increased, peaked at 80 °C, and then decreased, with different levels between MOF-801 and silica gel. Increasing the heating temperature from 70 °C to 80 °C improved the COP of the MOF-801 by 10% compared to 2% for silica-gel.

Consistently with the above, increasing the foam height increases the cyclic cooling capacity but increases the overall specific heat, which was more significant in MOF-801 of notably lower packing density. At large foam height, the domination of the high specific heat of copper foam was more influential, which led to a marginal difference in the COP, specifically at high heat source temperature.

The isotherm shape significantly influences the cooling capacity for MOF-801 and, consequently, its SCP_{vol}. At heat source temperatures between 70 °C and 85 °C, the desorption occurs at pressure ratios of $0.136 \leq P_{cond}/P_{bed} \leq 0.0734$. At this pressure ratio range, the equilibrium uptake/offtake for MOF-801 is slightly higher than that for silica gel. Therefore, the CC and the corresponding SCP_{vol} for MOF-801 are marginally higher than that for the SG-based system. By considering the variation in COP, the influence of the equilibrium uptake profile is more influential at shallow foam heights to the point of equal CC and the corresponding SCP_{vol} between 80 °C and 85 °C at foam height of 20 mm.

The above trends lead to a conclusion that low foam height persists in better initial cost-effectiveness with positive change in COP, SDWP and, most importantly, the cooling generated for a given physical footprint assessed by SCP_{vol}, yet an opposite effect was observed from the cooling capacity perspective.

4.7. The effect of heat sink temperature

Fig. 16 shows the influence of varying the cooling water inlet temperature (from 20 °C to 40 °C) and bed height (from 20 to 32 mm) on the system performance for MOF-801 and SG-packed bed into foamed bed. The cycle time, heating water inlet temperature and chilled water inlet temperature were maintained at 400 s, 85 °C and 15 °C, respectively.

Generally, and for the given system configuration, reducing the heat sink temperature enhances the effectiveness of the heat removed from the adsorbent bed during adsorption and condensation. Therefore, reducing the cooling water inlet temperature increases the net cyclic water vapour uptake by promoting the offtake during desorption/condensation and the uptake during adsorption/evaporation modes to fix the evaporator and desorption inlet temperature. The magnitude of MOF-801's adsorption isotherm varies depending on whether the desorption/condensation occurs where silica gel outperforms MOF-801 at pressure ratios below 7%. Therefore, the system's performance was generally enhanced by reducing the heat sink temperature, but the increment in the performance was reduced at temperatures below 30 °C for MOF-801. Such reduction in the increment is attributed primarily to the large thermal mass of MOF-801-packed beds, which is manifested by the low increment of COP and almost negligible change at temperatures below 30 °C. Besides, increasing the thermal mass and its predominant influence on slowing the system response and performance when using MOF-801 agrees with changing the heat source temperature.

It can be observed that at 20 mm foam height and in the case of MOF-801 and silica gel, the maximum SDWP of 12.78 m^3/(ton.day) and 11.8 m^3/(ton.day) occurred at a cooling water inlet temperature of 25 °C and 20 °C, respectively. The CC for MOF-801 outperformed silica-gel at cooling water inlet temperatures 30–40 °C at all bed heights, as the net cyclic water uptake was averagely 29% higher in the case of MOF-801. The CC of silica gel exceeded that of MOF-801 by decreasing the cooling water temperature from 30 °C to 20 °C with a more distinctive variation at shallow foam height as the cyclic water uptake was 13% higher. The CC for MOF-801 and silica-gel peaked at a cooling water inlet temperature of 20 °C, and the bed height of 32 mm was 38.8 kW for MOF-801 and 41.5 kW for silica-gel.

The SCP_{mass} of MOF-801 outperformed silica-gel for all the investigated cooling temperatures and bed height ranges, while the SCP_{vol} for MOF-801 exceeded those of silica-gel for the cooling temperature more than 30 °C. Given the combined effect of (i) increasing the cyclic water uptake by reducing the cooling water temperature and (ii) the domination of thermal mass for copper by increasing the foam height resulting in the slow thermal response, varying the cooling water temperature showed different trends for the systems utilised MOF-801 and silica gel. For instance, at $T_{cw} = 40$ °C, decreasing the bed height from 32

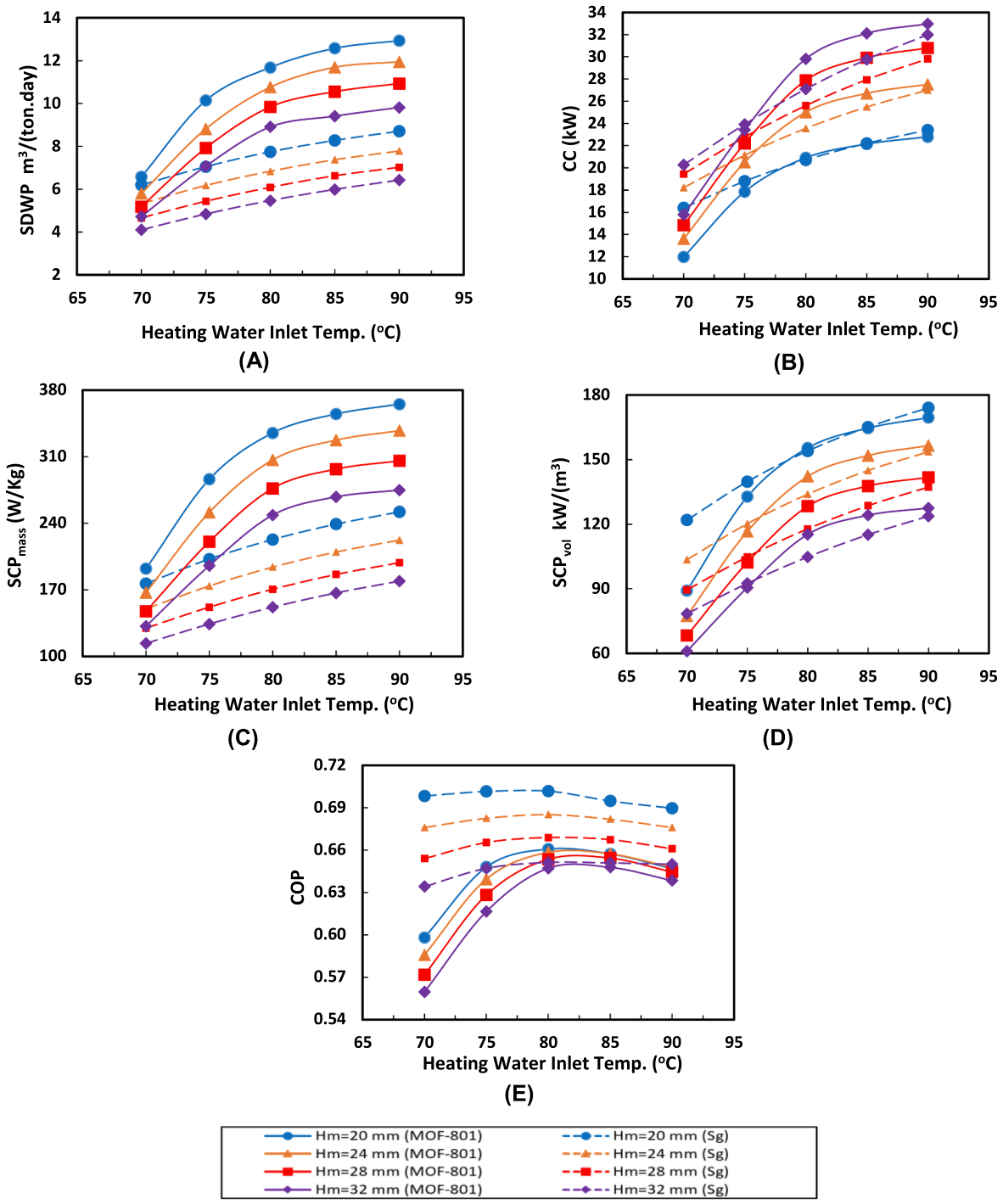

Fig. 15. The effect of the heating water inlet temperature and bed height on A-SDWP, B-CC, C-SCPmass, D-SCPvol and COP.

to 20 increased the SCP_{mass} and SCP_{vol} by 59% for MOF-801 compared to 43% for silica-gel. It is the opposite for $T_{cw} = 20$ °C; decreasing the bed height from 32 to 20 mm increased the SCP_{mass} and SCP_{vol} by 9% for MOF-801 compared to 50% for silica-gel. The maximum SCP_{mass} and SCP_{vol} for MOF-801 were 363 W/kg and 169 kW/m^3, which occurred at $T_{cw} = 25$ °C and bed height 20 mm, while the maximum SCP_{mass} and SCP_{vol} for silica-gel were 347 W/kg and 240 kW/m^3, which occurred at $T_{cw} = 20$ °C and bed height 20 mm.

Increasing the cooling water temperature decreased the system's COP gradually but plateaued at temperatures 20–30 °C for the MOF-801-based system. Generally, the increase of COP results from the higher cooling effect driven by the high cyclic uptake at low cooling temperatures, but the contradicting trends result from the high thermal mass of the MOF-801-based system. The COP of silica-gel- outperformed the MOF-801-based system at cooling temperatures of less than 32.5 °C for all bed heights. Decreasing the cooling water temperature from 40 °C to 20 °C improves the COP of the MOF-801 with an average of 11% compared to 37% for silica-gel. Both materials achieved their maximum COP at a bed height of 20 mm, reaching 0.654 for MOF-801 at $T_{cw} = 30$ °C compared to 0.744 for silica-gel at $T_{cw} = 20$ °C.

4.8. *The effect of the evaporator inlet water temperature*

Evaporation temperature is crucial. Its magnitude is decidable based

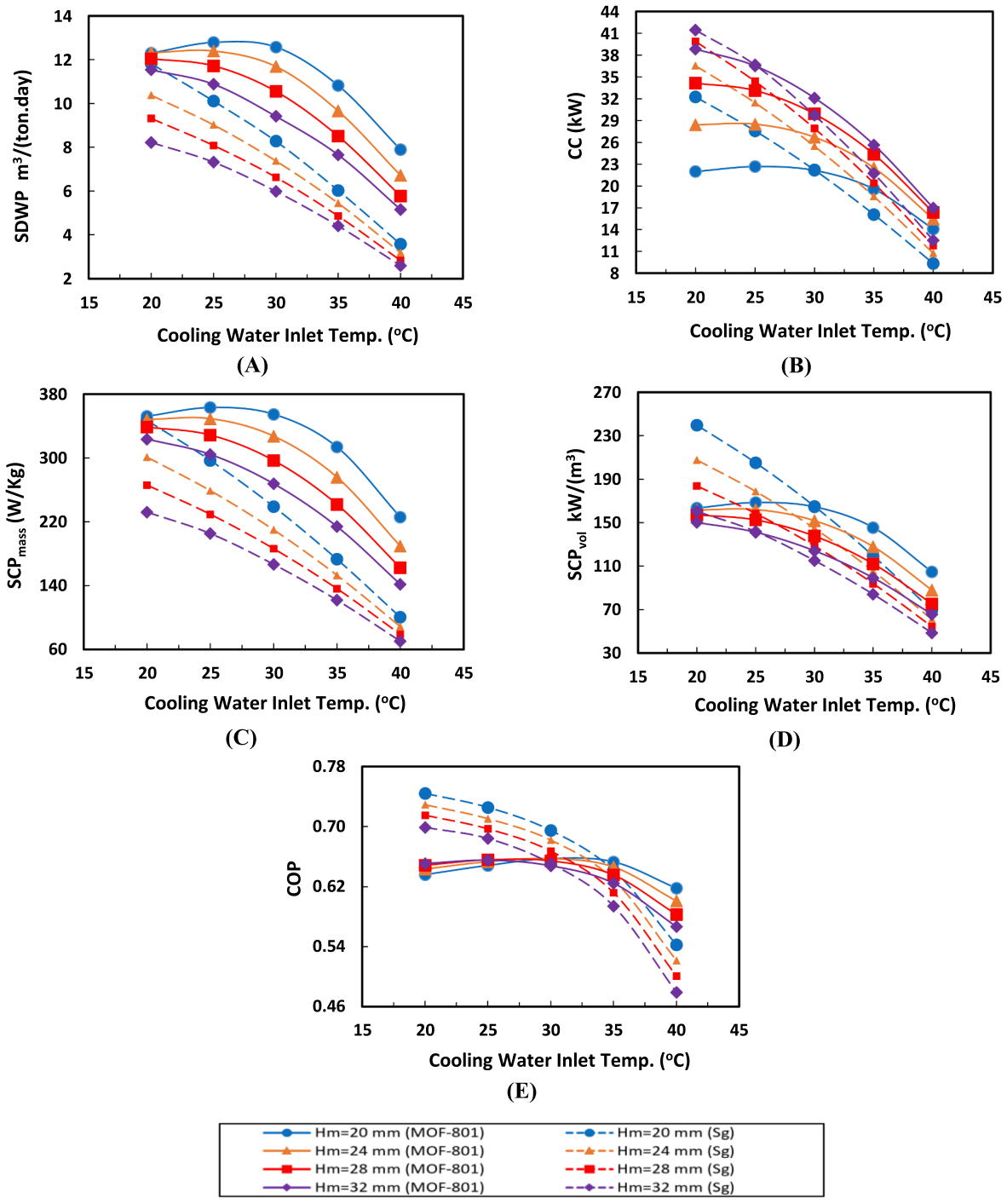

Fig. 16. The effect of the cooling water inlet temperature and bed height on A-SDWP, B-CC, C-SCPmass, D-SCPvol and COP.

on the application area, e.g., air conditioning and industrial processes (pharma, food, beverage), although the chilled water inlet temperature might be fixed during the operation. Low evaporation temperature is less concerning where the desalination is demanding or the adsorption cycle combined as a topping cycle into other power or cooling sub-systems. Therefore, this study was extended to provide insights into the impact of the evaporator inlet temperature on the system performance, which might benefit the system design and installation. Fig. 17 shows the impact of changing the evaporator inlet water temperature on the SDWP, CC, SCP_{mass}, SCP_{vol} and COP for MOF-801 and silica gel at a cycle time of 400 s, heat source temperature of 85 °C and cooling water temperature of 30 °C. The bed height varied from 20 mm to 32 mm. Based on the adsorption isotherm, the higher evaporation temperature leads to more cyclic water uptake and hence more magnitude of cooling.

It was observed that the SDWP for MOF-801 outperformed that for silica-gel within the investigated range of temperatures and foam height. Increasing the evaporator inlet water temperature from 10 °C to 30 °C increased the SDWP for MOF-801 and silica-gel by 59% and 153%, respectively, at bed height of 20 mm, but by higher increments of 86% and 120% at bed height 32 mm. The maximum SDWP occurred at bed height 20 mm and T_{chw} = 30 °C for both materials with 16.74 m^3/(ton.day) for MOF-801 compared to 15.47 m^3/(ton.day) for silica-gel.

Increasing the evaporator inlet water temperature from 10 °C to 30 °C showed a more distinctive influence on improving the CC for silica

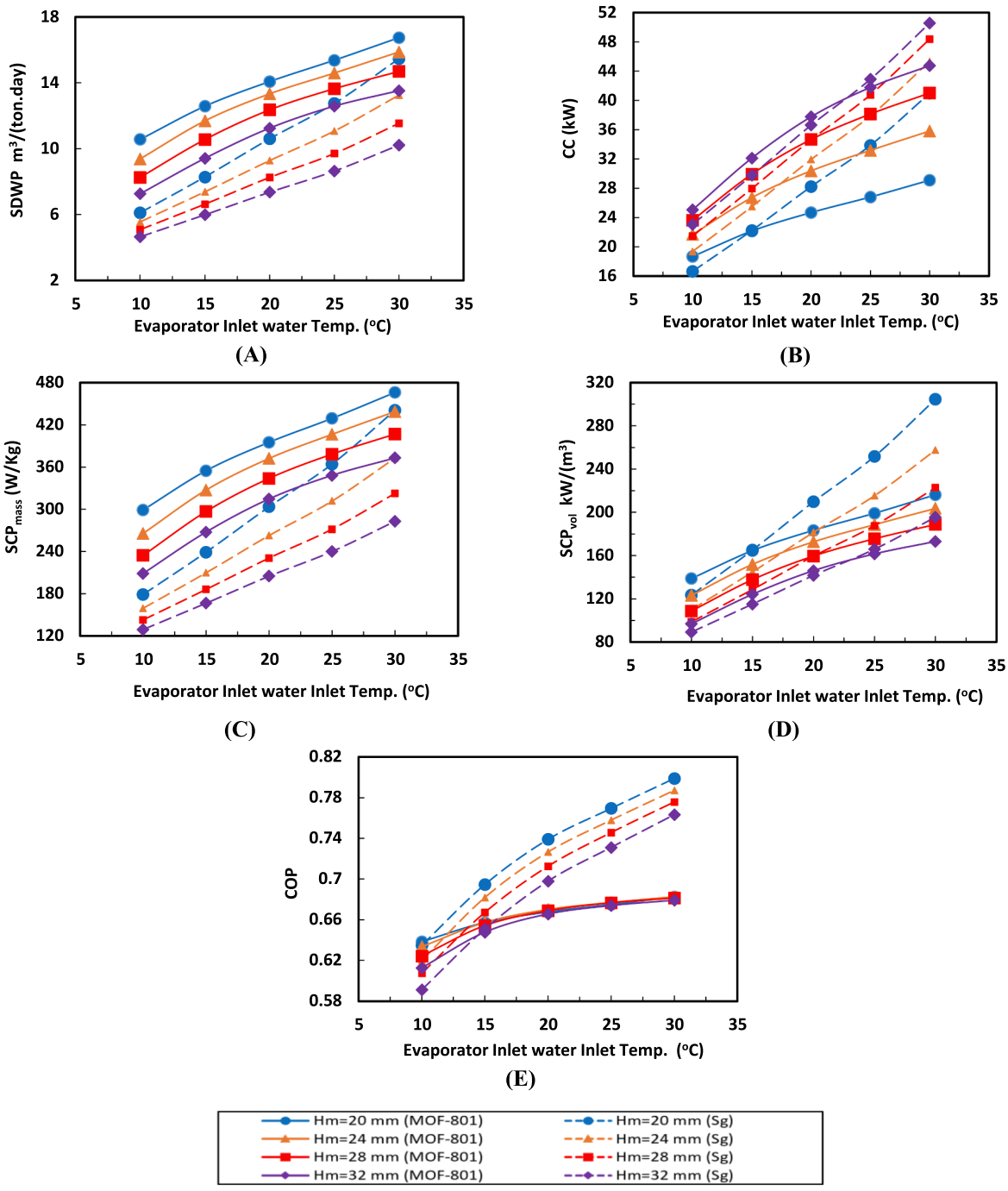

Fig. 17. The effect of the evaporator inlet water temperature and bed height on A-SDWP, B-CC, C-SCPmass, D-SCPvol and COP.

gel- compared to MOF-801-based systems. For example, the CC for MOF-801 and silica-gel increased by 56% and 147% at a bed height of 20 mm. It increased by 79% and 119%, respectively, at a bed height of 32 mm. The maximum CC achieved at bed height 32 mm and T_{chw} = 30 °C for both materials to be 44.7 kW for MOF-801 compared to 50.6 kW for silica-gel.

The SCP_{mass} for the MOF-801-based system outperformed that for the silica-gel-based system, while the SCP_{vol} values for MOF-801 exceeded those for silica gel at evaporator inlet water temperature less than 15 °C for the investigated bed heights. Increasing the evaporator inlet water temperature from 10 °C to 30 °C increased the SCP_{mass} and SCP_{vol} by 56% for MOF-801 compared to 147% for silica-gel at bed height 20 mm and with 79% for MOF-801 compared to 120% for silica gel at bed height 32 mm. The maximum SCP_{mass} and SCP_{vol} occurred at bed height 20 mm and T_{chw} = 30 °C for both materials to be 466 W/kg and 216 kW/m^3, respectively, for MOF-801 compared to 441 W/kg and 305 kW/m^3, respectively, for silica-gel.

Increasing the evaporator inlet water temperature from 10 °C to 30 °C significantly influenced the COP of the silica-gel-based system compared to the MOF-801-based system. Besides, changing the bed height marginally influenced the COP for MOF-801 for the evaporator inlet water temperatures of more than 20 °C, which contradicts the silica-gel-based system. For example, increasing the evaporator inlet water temperature from 10 °C to 30 °C at a bed height of 20 mm, increased the COP of MOF-801 by 7% compared to 26% for silica-gel. The maximum COPs achieved for both materials at T_{chw} = 30 °C were

Table 8
Global optimisation results considering 10 °C to 15 °C evaporative range.

Material based system	Optimum operation parameters				Optimum performance indicators				
	t_{cycle} (200 to 1000 s)	T_{hw} (70 to 100 °C)	T_{cw} (30 to 45 °C)	T_{chw} (10 to 15 °C)	SDWP)m^3/ton/day(	CC (kW)	SCP_{mass} (W/kg)	SCP_{vol} (kW/m^3)	COP
MOF-801	227.1	93.2	30.0	15.0	23.9	42.2	676.7	314.0	0.65
Silica-gel	228.1	92.4	30.0	15.0	15.9	43.2	464.7	321.1	0.69

0.683 for MOF-801 at a bed height of 24 mm and 0.8 for silica-gel at a bed height of 20 mm.

4.9. Multi-objective global optimisation

While the above parametric study developed an insight into influencing the operating conditions on the performance of the silica gel- and MOF-801-based systems, it is imperative to determine the optimal operating conditions for the best overall performance of the investigated systems. Therefore, multi-objective global optimisations were performed, including predefined ranges of operating parameters: cycle time varied from 200 s to 1000 s; the regeneration temperature varied from 70 °C to 100 °C; the T_{cw} varied from 30 °C to 45 °C. In addition, two ranges of evaporator inlet temperature were defined: from 10 °C to 15 °C prioritised the cooling temperature and from 10 °C to 25 °C prioritised the water desalination over cooling. At the 10–25 °C evaporator temperature range, a 5 °C deficit between the chilled water and cooling water inlet temperature was maintained to cohere with the practical operation to maintain the driving pressure difference between the condenser and evaporator. The foamed bed height was fixed at 20 mm, representing the maximum SCP_{mass}, SCP_{vol}, and SDWP in the parametric studies across the investigated cases.

The genetic algorithm (GA) optimisation technique was applied, and a composited objective function, shown in the equation (26), was developed to undertake multi-objective global optimisation employing the MATLAB platform. The multi-objective function was developed to maximise SCP_{mass} and COP equally, and the objective function was developed to represent such a physical phenomenon numerically. However, other weighings of SCP_{mass} and COP in the objective functions might be considered according to the application (e.g., demanding more cooling and water production at the expense of the COP or visa versa). The SCP_{mass}'s unit of kW/kg was selected to arithmetically have the same COP's order of magnitude hence unpolarised the solution toward an indicator at the expense of the other. As aforementioned, SCP_{mass} is a strong function of the cyclic water uptake and maximising it will proportionally maximise the SDWP and SCP_{vol} to an extent. However, SCP_{vol} represents more of the system's form factor.

$$GA\_bjective = 50\%COP + 50\%SCP_{mass}(kW/kg) \quad (27)$$

In this study, the GA's population for each parameter was 20. Therefore, the number of stall generations was 20, and the crossover fraction was 0.8, which was previously recommended by Rezk et al. [62].

The outcomes of the global optimisation within the 10 °C to 15 °C evaporative temperature range are populated in Table 8. The optimal operating conditions for silica gel- and MOF-801-based systems are very close. However, the corresponding SDWP and SCP_{mass} of the MOF-801-based system outperform their counterparts of the SG-based system by 50.3% and 45.6%, respectively. These enhancements are coupled with a reduction in the SCP_{vol} and COP of the MOF-801-based system compared to the SG-based system by 2.2% and 6.5%, respectively.

The outcomes of the global optimisation within the 10 °C to 25 °C evaporative temperature range are populated in Table 9. Building on the parametric study that showed the enhancement of the system's performance by increasing the chilled water inlet temperature, the optimal chilled water inlet temperature was found to be 25 °C with variation in the other operating conditions. On the one hand, in the 10 °C to 25 °C evaporative temperature range and, at optimum operating conditions, the SDWP and SCP_{mass} of the MOF-801-based system outperformed their counterparts of SG-based system by 38.1% and 35.9%, respectively. On the other hand, the SCP_{vol} and COP of the MOF-801-based system compared to the SG-based system decreased by 8.8 % and 16.8%, respectively. It is noticed that the MOF-801-based system requires a lower cycle time of 226 s and a higher regeneration temperature of 93.7 °C, compared to the SG-based system, to maximise its overall performance. To relate to the undertaken parametric study: the optimal cycle time for both systems achieved the best COP at the ramping-up portion of the curve and SCP_{mass} near the peak; the optimal heating water temperature for both systems achieved the best COP at the gradual ramping-down portion of the curve and SCP_{mass} near the peak.

5. Conclusions

This article investigated the influence of the operating conditions and physical parameters on the overall ADCD system utilising the state-of-the-art adsorbent MOF-801 packed into the emerging copper-foamed adsorbent bed. The fundamental knowledge from the parametric study enabled undertaking multi-objective global optimisation to identify the optimal operating conditions for maximising multiple performance indicators. Accordingly, the following can be concluded.

- Employing MOF-801 into the copper-foam bed of the ADCD system considerably boosted the SDWP and SCP_{mass} compared to the counterpart SG-based, almost at all operating conditions. However, under the same operating conditions, the COP of the MOF-801-based system was less than the SG-based system. Lowering the evaporator inlet temperature enabled the MOF-801-based system to attain SDWP and SCP_{mass} higher than the SG-based system while attaining almost the same COP for both systems.

- The global multi-objective optimisation proved its ability to deal with a wide range of operating conditions. It can incorporate more than one objective using weighting factors representing the users' greatly demanded parameters. Optimising different evaporator inlet

Table 9
Global optimisation results considering 10 °C to 25 °C evaporative range.

Material based system	Optimum operation parameters				Optimum performance indicators				
	t_{cyc} (200 to 1000 s)	T_{hw} (70 to 100 °C)	T_{cw} (30 to 45 °C)	T_{chw} (10 to 25 °C)	SDWP)m^3/ton/day(	CC (kW)	SCP_{mass} (W/kg)	SCP_{vol} (kW/m^3)	COP
MOF-801	226.1	93.7	32.5	25.0	29.7	51.8	830.8	385.5	0.667
Silica-gel	312.6	85.7	30.4	25.0	21.5	56.8	611.5	422.5	0.802

temperature ranges revealed higher max-SCP_{mass} and max-SDWP but lower max-SCP_{vol} and max-COP for MOF-801-based systems than the SG-based system. The corresponding optimal cycle time for the MOF-801-based system was shorter than the SG-based system.

The future work will emphasise broadening the system optimisation to map the optimal operational range at different scenarios of the composited objective function.

Declaration of Competing Interest

The authors declare that they have no known competing financial interests or personal relationships that could have appeared to influence the work reported in this paper.

Data availability

Data will be made available on request.

References

[1] 2030 Water Resources Group, 2014 Annual Report: Building Partnerships for Water Security.
[2] J. Kölbel, C. Strong, C. Noe, P. Reig, Mapping public water management by harmonizing and sharing corporate water risk information, 2018.
[3] International Energy Agency (IEA), Introduction to the water-energy nexus, Paris (2020).
[4] P.G. Youssef, R.K. Al-Dadah, S.M. Mahmoud, Comparative analysis of desalination technologies, Energy Proc. 61 (2014) 2604–2607, https://doi.org/10.1016/j.egypro.2014.12.258.
[5] T. Mezher, et al., Techno-economic assessment and environmental impacts of desalination technologies, Desalination. 266 (2010), https://doi.org/10.1016/j.desal.2010.08.035.
[6] J. Cotruvo, P. Payment, N. Voutchkov, J. Fawell, S. Lattemann, D. Cunliffe, (Eds.), Desalination Technology: Health and Environmental Impacts (1st ed.), 2010.
[7] International Energy Agency (IEA), World Energy Outlook 2016, IEA, Paris (2016).
[8] International Energy Agency (IEA), The Future of Cooling, Paris (2018).
[9] EPA, Protecting our Climate by Reducing Use of Hydrofluorocarbons. (2022).
[10] B.B. Saha, et al., Fundamental and application aspects of adsorption cooling and desalination, Appl. Therm. Eng. 97 (2016) 68–76, https://doi.org/10.1016/j.applthermaleng.2015.09.113.
[11] A.S. Alsaman, et al., Performance evaluation of a solar-driven adsorption desalination-cooling system, Energy. 128 (2017) 196–207, https://doi.org/10.1016/j.energy.2017.04.010.
[12] R. Raj, V. Baiju, Thermodynamic analysis of a solar powered adsorption cooling and desalination system, Energy Proc. 158 (2019) 885–891, https://doi.org/10.1016/j.egypro.2019.01.226.
[13] R.Z. Wang, et al., Solar sorption cooling systems for residential applications: Options and guidelines, Int J Refrig. 32 (4) (2009) 638–660, https://doi.org/10.1016/j.ijrefrig.2009.02.005.
[14] Q.W. Pan, R.Z. Wang, Study on operation strategy of a silica gel-water adsorption chiller in solar cooling application, Solar Energy. 172 (2018) 24–31, https://doi.org/10.1016/j.solener.2018.03.062.
[15] P. Goyal, et al., Adsorption refrigeration technology – An overview of theory and its solar energy applications, Renewable and Sustainable Energy Reviews. 53 (2016) 1389–1410, https://doi.org/10.1016/j.rser.2015.09.027.
[16] M.B. Elsheniti, et al., Experimental evaluation of a solar two-bed lab-scale adsorption cooling system, Alex. Eng. J. 60 (3) (2021) 2747–2757, https://doi.org/10.1016/j.aej.2021.01.024.
[17] K. Ng, et al., Study on a waste heat-driven adsorption cooling cum desalination cycle, Int J Refrig-revue Internationale Du Froid 35 (2012) 685–693, https://doi.org/10.1016/j.ijrefrig.2011.01.008.
[18] K. Thu, et al., Performance investigation of a waste heat-driven 3-bed 2-evaporator adsorption cycle for cooling and desalination, Int. J. Heat Mass Transf. 101 (2016) 1111–1122, https://doi.org/10.1016/j.ijheatmasstransfer.2016.05.127.
[19] S. Stefański, et al., Applicability of adsorption cooling/desalination systems driven by low-temperature waste heat, IOP Conference Series: Earth and Environmental Science. 214 (2019), 012126, https://doi.org/10.1088/1755-1315/214/1/012126.
[20] M. Hamdy, et al., An overview on adsorption cooling systems powered by waste heat from internal combustion engine, Renewable and Sustainable Energy Reviews. 51 (2015) 1223–1234, https://doi.org/10.1016/j.rser.2015.07.056.
[21] L.Z. Zhang, Design and testing of an automobile waste heat adsorption cooling system, Appl. Therm. Eng. 20 (2000) 103–114, https://doi.org/10.1016/S1359-4311(99)00009-5.
[22] W. Chekirou, et al., Dynamic modelling and simulation of the tubular adsorber of a solid adsorption machine powered by solar energy, Int J Refrig. 39 (2014) 137–151, https://doi.org/10.1016/j.ijrefrig.2013.11.019.
[23] Gautam and S. Sahoo,, Effects of geometric and heat transfer parameters on adsorption–desorption characteristics of CO2-activated carbon pair. Clean Technol Environ, Policy. 23 (2021), https://doi.org/10.1007/s10098-020-01866-3.
[24] S. Narayanan, et al., Optimization of adsorption processes for climate control and thermal energy storage, IInt. J. Heat Mass Transf. 77 (2014) 288–300, https://doi.org/10.1016/j.ijheatmasstransfer.2014.05.022.
[25] M.B. Elsheniti, M.A. Hassab, A.-E. Attia, Examination of effects of operating and geometric parameters on the performance of a two-bed adsorption chiller, Appl. Therm. Eng. 146 (2019) 674–687, https://doi.org/10.1016/j.applthermaleng.2018.10.043.
[26] Fopah Lele, A., et al. Thermal conductivity measurement of salt hydrate as porous material using calorimetric (DSC) method. in Eighth World Conference on Experimental Heat Transfer, Fluid Mechanics and Thermodynamics 2013. Lisbon, Portugal.
[27] D.S. Smith, et al., Thermal conductivity of porous materials, J. Mater. Res. 28 (17) (2013) 2260–2272, https://doi.org/10.1557/jmr.2013.179.
[28] ul Qadir, N., S.A.M. Said, and R.B. Mansour,, Modeling the performance of a two-bed solar adsorption chiller using a multi-walled carbon nanotube/MIL-100(Fe) composite adsorbent, Renewable Energy. 109 (2017) 602–612, https://doi.org/10.1016/j.renene.2017.03.077.
[29] X. Zheng, Z. Lin, B.Y. Xu, Thermal conductivity and sorption performance of nano-silver powder/FAPO-34 composite fin, Appl. Therm. Eng. 160 (2019), 114055, https://doi.org/10.1016/j.applthermaleng.2019.114055.
[30] Z. Jin, et al., Comparison on Thermal Conductivity and Permeability of Granular and Consolidated Activated Carbon for Refrigeration, Chin. J. Chem. Eng. 21 (6) (2013) 676–682, https://doi.org/10.1016/S1004-9541(13)60525-X.
[31] I.I. El-Sharkawy, et al., A study on consolidated composite adsorbents for cooling application, Appl. Therm. Eng. 98 (2016) 1214–1220, https://doi.org/10.1016/j.applthermaleng.2015.12.105.
[32] R.H. Mohammed, et al., Performance evaluation of a new modular packed bed for adsorption cooling systems, Appl. Therm. Eng. 136 (2018) 293–300, https://doi.org/10.1016/j.applthermaleng.2018.02.103.
[33] S. Stefański, et al., Adsorption bed configurations for adsorption cooling application, E3S Web of Conferences. 108 (2019) 01010, https://doi.org/10.1051/e3sconf/201910801010.
[34] M. Mohammadzadeh Kowsari, H. Niazmand, M.M. Tokarev, Bed configuration effects on the finned flat-tube adsorption heat exchanger performance: Numerical modeling and experimental validation, Appl. Energy. 213 (2018) 540–554, https://doi.org/10.1016/j.apenergy.2017.11.019.
[35] A.A. Askalany, et al., Effect of improving thermal conductivity of the adsorbent on performance of adsorption cooling system, Appl. Therm. Eng. 110 (2017) 695–702, https://doi.org/10.1016/j.applthermaleng.2016.08.075.
[36] H. Demir, M. Mobedi, S. Ulku, The use of metal piece additives to enhance heat transfer rate through an unconsolidated adsorbent bed, Int J Refrig. 33 (2010), https://doi.org/10.1016/j.ijrefrig.2009.12.032.
[37] K.C. Chan, et al., Enhancing the performance of a zeolite 13X/CaCl2–water adsorption cooling system by improving adsorber design and operation sequence, Energy Build. 158 (2018) 1368–1378, https://doi.org/10.1016/j.enbuild.2017.11.040.
[38] S.K. Henninger, et al., Novel Sorption Materials for Solar Heating and Cooling, Energy Procedia. 30 (2012) 279–288, https://doi.org/10.1016/j.egypro.2012.11.033.
[39] Y.I. Aristov, et al., A family of new working materials for solid sorption air conditioning systems, Appl. Therm. Eng. 22 (2) (2002) 191–204, https://doi.org/10.1016/S1359-4311(01)00072-2.
[40] R.H. Mohammed, et al., Metal-organic frameworks in cooling and water desalination: Synthesis and application, Renewable and Sustainable Energy Reviews. 149 (2021), 111362, https://doi.org/10.1016/j.rser.2021.111362.
[41] S. Hong, et al., Characteristics of FAM-Z01compared to silica gels in the performance of an adsorption bed, Appl. Therm. Eng. 104 (2016), https://doi.org/10.1016/j.applthermaleng.2016.05.058.
[42] B. Teo, A. Chakraborty, W. Fan, Improved adsorption characteristics data for AQSOA types zeolites and water systems under static and dynamic conditions, Microporous Mesoporous Mater. 242 (2017), https://doi.org/10.1016/j.micromeso.2017.01.015.
[43] M.F. de Lange, et al., Adsorption-Driven Heat Pumps: The Potential of Metal-Organic Frameworks, Chemical Reviews. 115 (22) (2015) 12205–12250, https://doi.org/10.1021/acs.chemrev.5b00059.
[44] J. Do, et al., Hydrothermal synthesis and application of adsorbent coating for adsorption chiller, Progress in Organic Coatings. 128 (2019) 59–68, https://doi.org/10.1016/j.porgcoat.2018.12.011.
[45] M. Shaaban, et al., Performance investigation of adsorption cooling and desalination systems employing thermally enhanced copper foamed bed coated with SAPO-34 and CPO-27(Ni), Appl. Therm. Eng. (2022), 118056, https://doi.org/10.1016/j.applthermaleng.2022.118056.
[46] J.M. Pinheiro, et al., Copper foam coated with CPO-27(Ni) metal–organic framework for adsorption heat pump: Simulation study using OpenFOAM, Appl. Therm. Eng. 178 (2020), 115498, https://doi.org/10.1016/j.applthermaleng.2020.115498.
[47] A. Freni, et al., Zeolite synthesised on copper foam for adsorption chillers: A mathematical model, Microporous Mesoporous Mater. 120 (3) (2009) 402–409, https://doi.org/10.1016/j.micromeso.2008.12.011.
[48] R.H. Mohammed, et al., Performance enhancement of adsorption beds with silica-gel particles packed in aluminum foams, Int J Refrig. 104 (2019) 201–212, https://doi.org/10.1016/j.ijrefrig.2019.03.013.
[49] H. Furukawa, et al., Water Adsorption in Porous Metal-Organic Frameworks and Related Materials, J. Am. Chem. Soc. 136 (11) (2014) 4369–4381, https://doi.org/10.1021/ja500330a.

[50] M.V. Solovyeva, et al., MOF-801 as a promising material for adsorption cooling: Equilibrium and dynamics of water adsorption, Energy Convers. 174 (2018) 356–363, https://doi.org/10.1016/j.enconman.2018.08.032.
[51] H. Kim, et al., Water harvesting from air with metal-organic frameworks powered by natural sunlight, Science. 356 (6336) (2017) 430–434, https://doi.org/10.1126/science.aam8743.
[52] H. Kim, et al., Adsorption-based atmospheric water harvesting device for arid climates, Nature Communications. 9 (1) (2018) 1191, https://doi.org/10.1038/s41467-018-03162-7.
[53] S. Furmaniak, et al., Heterogeneous Do–Do model of water adsorption on carbons, J. Colloid Interface Sci. 290 (1) (2005) 1–13, https://doi.org/10.1016/j.jcis.2005.07.043.
[54] E. Elsayed, et al., Adsorption cooling system employing novel MIL-101(Cr)/CaCl2 composites: Numerical study, Int J Refrig. 107 (2019) 246–261, https://doi.org/10.1016/j.ijrefrig.2019.08.004.
[55] A. Rezk, et al., Investigation of Ethanol/metal organic frameworks for low temperature adsorption cooling applications, Appl. Energy. 112 (2013) 1025–1031, https://doi.org/10.1016/j.apenergy.2013.06.041.
[56] J. Wang, X. Guo, Adsorption isotherm models: Classification, physical meaning, application and solving method, Chemosphere. 258 (2020), 127279, https://doi.org/10.1016/j.chemosphere.2020.127279.
[57] A. Rezk, et al., Characterisation of metal organic frameworks for adsorption cooling, IInt. J. Heat Mass Transf. 55 (25) (2012) 7366–7374, https://doi.org/10.1016/j.ijheatmasstransfer.2012.07.068.
[58] B.B. Saha, E.C. Boelman, T. Kashiwagi, Computational analysis of an advanced adsorption-refrigeration cycle, Energy. 20 (10) (1995) 983–994, https://doi.org/10.1016/0360-5442(95)00047-K.
[59] H. Chua, et al., Modeling the performance of two-bed, silica gel-water adsorption chillers, Int J Refrig. 22 (2008) 194–204, https://doi.org/10.1016/S0140-7007(98)00063-2.
[60] A. Rezk, et al., Effects of contact resistance and metal additives in finned-tube adsorbent beds on the performance of silica gel/water adsorption chiller, Appl. Therm. Eng. 53 (2) (2013) 278–284, https://doi.org/10.1016/j.applthermaleng.2012.04.008.
[61] A.R.M. Rezk, R.K. Al-Dadah, Physical and operating conditions effects on silica gel/water adsorption chiller performance, Appl. Energy. 89 (1) (2012) 142–149, https://doi.org/10.1016/j.apenergy.2010.11.021.
[62] M.B. Elsheniti, et al., Performance of a solar adsorption cooling and desalination system using aluminum fumarate and silica gel, Appl. Therm. Eng. 194 (2021), 117116, https://doi.org/10.1016/j.applthermaleng.2021.117116.
[63] M.G. Gado, et al., Parametric Study of an Adsorption Refrigeration System Using Different Working Pairs %J International Conference on Aerospace Sciences and Aviation Technology. 17 (aerospace sciences & aviation technology, ASAT - 17 – April 11 - 13, 2017) (2017) 1-15. 10.21608/asat.2017.22455.